Available online at www.sciencedirect.com
ScienceDirect
Lithos 99 (2007) 289–311
LITHOS
www.elsevier.com/locate/lithos

Bulk-rock geochemistry and plagioclase zoning in lavas exposed along the northern flank of the Western Blanco Depression (Northeast Pacific): Insight into open-system magma chamber processes

Carole Cordier *, Martial Caroff, Thierry Juteau, Corinne Fleutelot, Christophe Hémond, Marion Drouin [1], Joseph Cotten, Claire Bollinger

Laboratoire des Domaines Océaniques (UMR6538), Université de Bretagne Occidentale et Centre Nationale de la Recherche Scientifique, Institut Universitaire Européen de la Mer (IUEM), Place Copernic, 29280 Plouzané, France

Received 17 May 2006; accepted 15 June 2007
Available online 23 June 2007

Abstract

The present study is based on a set of lavas and crosscutting dikes collected by dives along detailed vertical transects on the northern flank of the western part of the Blanco Transform Fault, Northeast Pacific. The studied area consists of a small basin, the Western Blanco Depression (WBD), extending from the southern end of the Juan de Fuca ridge to a pseudofault trace 60 km eastward. The Northern Scarp of the WBD comprises a volcanic unit overlying a sheeted-dike complex. Major and trace element data, coupled with Sr–Nd isotope ratios, reveal a two-component mantle source, composed by an isotopically depleted matrix variably veined by more enriched material. One chemical group (NS2), indistinguishable from the other Northern Scarp samples on the basis of trace element data, has an unusually depleted isotopic composition typical of a nearly pure mantle end-member. Some cogenetic samples of the Northern Scarp have been used to constrain the differentiation modalities. Anorthite and MgO content profiles in plagioclase xenocrysts and phenocrysts reveal (i) the existence of H_2O-bearing evolved melts in the mushy zones and (ii) the occurrence of mixing process between these melts and anhydrous mafic liquids. The hydration is supported by other petrographic features such as high magmatic fO_2 values, calculated from Fe–Ti oxide pairs, and the presence of pyroxene inclusions in plagioclase phenocrysts. Mixing, consistent with the existence of Ni-rich ferrobasalts, is interpreted to be the consequence of the reservoir refilling by mafic liquids (Mg#=70). These petrological and geochemical evidences are combined with the evolution of Mg# with depth to suggest a periodic open-system magma chamber evolution beneath the southern end of the Juan de Fuca ridge.
© 2007 Elsevier B.V. All rights reserved.

Keywords: Transform fault; Plagioclase zoning; Crystallization; Hydration; Mushy zone; Magma mixing

1. Introduction

Transform zones belong to oceanic plate frontiers, sometimes separating two geochemically contrasted segments and revealing mantle segmentation (Sinton et al., 1991; Smith et al., 1998; Niu et al., 2001). Between transforms and beneath fast and intermediate spreading

* Corresponding author. Tel.: +33 29 8017289; fax: +33 29 8016620.
E-mail address: carole.cordier@sdt.univ-brest.fr (C. Cordier).
[1] Present address: Laboratoire de Tectonophysique, Université Montpellier II, 34095 Montpellier Cedex, France.

0024-4937/$ - see front matter © 2007 Elsevier B.V. All rights reserved.
doi:10.1016/j.lithos.2007.06.009

ridges, the axial magma reservoirs are thought to be composite with a thin melt lens overlying a large zone of crystal mush (Sinton and Detrick, 1992; Singh et al., 1998; Dunn and Toomey, 2000). Geological and geochemical studies have shown that these reservoirs are generally long-lived and periodically refilled (e.g. Caroff et al., 1997; Lagabrielle and Cormier, 1999). Close to or within the transform zones, fractionated basalts (ferrobasalts) are frequently sampled (Sinton et al., 1983; Juteau et al., 1995; Cotsonika et al., 2005; Stakes et al., 2006).

In this study, we focus on the Northern Scarp of the Western Blanco Transform Zone (southern end of the Juan de Fuca ridge). Contrary to some other transform zones, the outcropping crustal section has been only slightly tectonized. Thus, the Northern Scarp provides a remarkable petrographic window into the upper oceanic crust down to the sheeted-dike complex and an opportunity to study the temporal variations of the lava composition through the volcanic pile. New geochemical data (major and trace elements, Sr–Nd isotopic ratios) from the extrusive unit outcropping along the Western Blanco Depression are used to compare the chemistry of lavas from both flanks. Once determined which samples are cogenetic, we focus on the differentiation of the northern flank lavas using a detailed study of the geochemistry and plagioclase zoning of remarkable samples collected along one dive.

2. Geological setting

2.1. The Blanco Transform Fault and the Western Blanco Depression

The Blanco Transform Fault (BTF) is a 360-km-long, left-stepping, dextrally-slipping fault that bounds the north of the Gorda ridge and the south of the Cleft segment of the Juan de Fuca ridge (Fig. 1, inset). The BTF comprises five segments roughly perpendicular to the Juan de Fuca ridge and separated by small basins. The Western Blanco Depression (WBD) extends parallel to the BTF from the southern end of the Juan de Fuca ridge

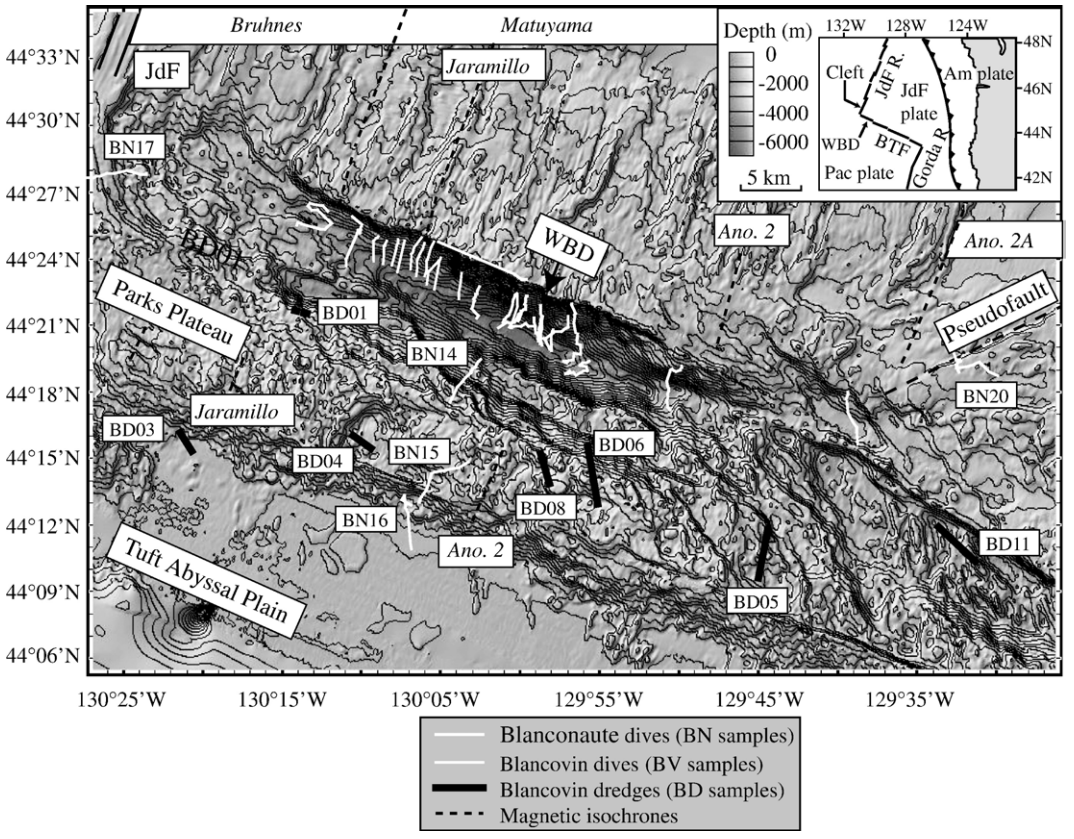


Fig. 1. Bathymetric map of the Western Blanco Depression (WBD) with superimposed magnetic isochrones (Embley and Wilson, 1992). Submersible dives and dredge paths from the Blanconaute and Blancovin cruises are reported. The dives and dredges not shown in Fig. 2 are given here. Inset: location map of the WBD in the NE Pacific. JdF plate: Juan de Fuca plate; Am plate: American plate; Pac plate: Pacific plate; JdF R.: Juan de Fuca ridge; Gorda R.: Gorda ridge.

to a pseudofault trace 60 km to the east (Fig. 1). It is a N112°E-trending 10 km-wide trough, which reaches a maximum depth of 4860 m. The pseudofault trace indicates earlier southward propagation of the Juan de Fuca ridge. The most recent propagating rift reached the BTF 1.4 My ago (Wilson et al., 1984; Embley and Wilson, 1992). For 1.4 My, spreading has been accommodated by accretion. Thus, the lithosphere presently exposed along the Northern Scarp originated to the north of the ridge-transform intersection, in the southern end of the Cleft segment at an intermediate full spreading rate of 56 mm/yr (Wilson, 1992).

2.2. Lithology of the crust exposed along the WBD

The Northern Scarp of the WBD truncates the ridge-parallel lineated magnetic anomalies formed at the Juan de Fuca ridge (from Brunhes to Anomaly 2A, Tivey, 1994). It is a linear cliff (dip 45–50°S) with continuous outcrops reaching up to hundreds of meters and separated by small steps covered with talus debris and sediments. Along this scarp, a 900–1000 m-thick volcanic unit is separated from a sheeted-dike complex by a slight drop in the cliff slope (Juteau et al., 1995; Karson et al., 2002). The volcanic unit consists mainly of basaltic pillow-lavas, with a few massive flows, intruded by sparse feeder dikes. The lava flows dip northwesterly (toward the spreading axis) gradually more with depth (Karson et al., 2002). This dip evolution with depth has been attributed to a rapid subsidence beneath the spreading axis (1–3 km), which quickly diminishes off-axis (Karson et al., 2002; Pollock et al., 2005). Late top flows, channeled away from the axis, underwent a more moderated subsidence. The dikes of the sheeted complex roughly strike north–northeast and typically dip of 30–50° to the southeast (Karson et al., 2002). They show evidence of an intensive hydrothermal alteration, with development of numerous whitish veins at the dike joints (Manac'h et al., 1999). A few massive coarse-grained rocks have been observed at the bottom of the scarp (Fig. 2). In the neighboring dives BN24 and BV2963 (spaced by 100 m), the lithological succession is complicated by tectonic offsets due to normal faulting and the transition between sheeted dikes and extrusives is crossed twice (Fig. 2). Based on the repetition of this transition, the collapse of the lower block in both dives can be estimated at 550–700 m. Furthermore, due to their steepness, the slopes are gravitationally unstable and the dives BN07, BN08 and BN10 have sampled cliff sectors affected by a major landslide (0.85 km^3). The slide block has slipped down over 600 m (Juteau et al., 1995).

To the south, the WBD is flanked by the Parks Plateau, lying at present on the Pacific plate. It is a 1650 m-high, 12 km-wide, and 70 km-long structure. The lithologic succession of the south wall of the WBD (northern flank of the Parks Plateau) differs from the

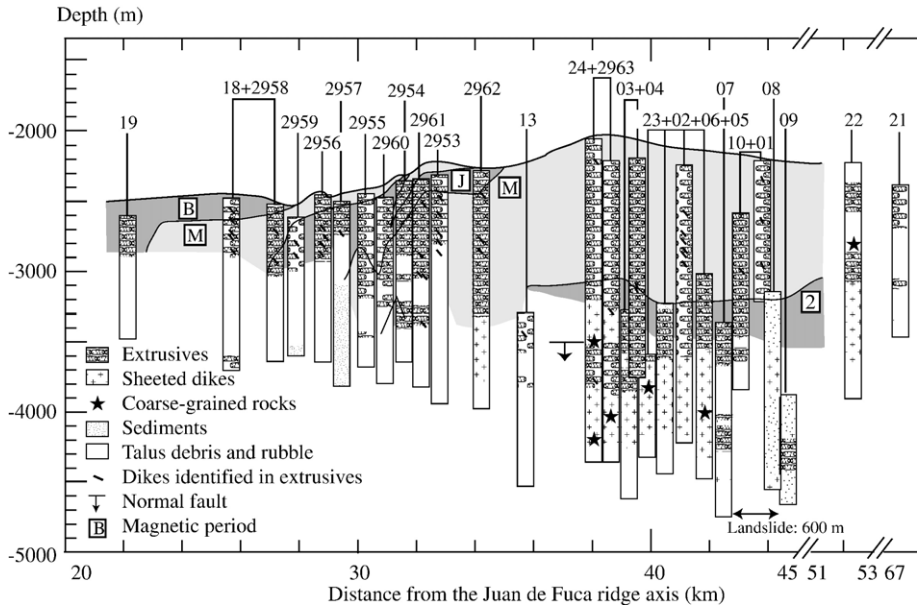


Fig. 2. Schematic representation of the lithologies observed along the Northern Scarp of the WBD superimposed on the magnetic cross section modified after Tivey (1996) and Tivey et al. (1998). Normal polarity crust is shaded in light gray (M: Matuyama) and is separated by isochrones from inverse polarity crust in dark gray (B: Brunhes, J: Jaramillo, 2: Anomaly 2). The dives are labeled at the top of the scarp (29XX names referring to the Alvin dives, the other names to the Nautile dives) and the dives that will be combined together in Section 7 are linked by horizontal lines.

Northern Scarp by the lack of sheeted-dike complex and the presence of hyaloclastites in the lower part of the scarp. The top of the Parks Plateau is capped by small, isolated volcanoes, out of which erupted the lava flows covering its southern flank.

Two models have been proposed for the geodynamical evolution of the WBD area (Dauteuil, 1995):

(1) The southern flank (Parks Plateau) would correspond to a seamount. This model is supported by (i) the present position of the plateau, at the edge of a transform fault where off-axis magmatism is frequently observed; (ii) the abundance of small volcanic edifices in its central part and the lack of any sheeted-dike complex; and (iii) its elongated morphology suggesting a volcanic origin (Fig. 1).
(2) Both flanks of the WBD would have evolved together on the Juan de Fuca plate until 0.4–0.2 My. Then, minor changes in relative motion between Juan de Fuca and Pacific plates would have caused a northward jump of the transform, from the southern flank of the Parks Plateau to the present-day location along the northern flank of the WBD (Embley and Wilson, 1992; Dauteuil, 1995; Juteau et al., 1995). This model is supported by (i) the shift of the seafloor magnetic anomalies between the two sides of the WBD (Fig. 1); (ii) the similar average depth of the Parks Plateau and the Juan de Fuca plate (Fig. 1); and (iii) the similar trend of the tectonic structures in both the Parks Plateau and the Juan de Fuca plate.

2.3. Temporal and spatial relationships along the Northern Scarp

Along the Northern Scarp, the temporal evolution of the lava chemistry can be investigated by studying lavas both horizontally and vertically. Horizontally, lavas become older with increasing distance to the Juan de Fuca ridge, consistently with the succession of measured seafloor magnetic boundaries (Fig. 1) and with the increasing damage of the flow morphology eastward. The vertical succession has a temporal significance only throughout the extrusives (Fig. 2). Lava tilting (Karson et al., 2002) and magnetization profiles versus depth (Tivey et al., 1998) suggest that the isochrones form curved trends that dip toward the Juan de Fuca ridge. Consequently, each overlying lava was emplaced further off-axis than the one below it. Even if the dive paths are not perpendicular to the isochrones, the vertical succession of lavas is thought to record increasing age lavas with depth (Pollock et al., 2005).

3. Petrology of the lavas and crosscutting dikes from the Northern Scarp

3.1. Sampling

The crust exposed along the Northern Scarp of the WBD was the object of several geological, geophysical, and geochemical studies (Delaney et al., 1987; Gaetani et al., 1995; Juteau et al., 1995; Tivey, 1996; Fleutelot, 1997; Naidoo, 1998; Tivey et al., 1998; Manac'h et al., 1999; Karson et al., 2002; Pollock et al., 2005). They were all based on samples and observations achieved through three cruises between 1987 and 1995. The present study uses samples collected from the extrusive unit (lavas and crosscutting dikes) during the Blanconaute (1991) and Blancovin (1995) programs. During the Blanconaute cruise, twenty Nautile dives sampled the Northern Scarp (acronym BN ahead of the sample numbers) from the Juan de Fuca ridge axis (BN17) to the pseudofault (BN20, Figs. 1 and 2). Three additional Blanconaute dives were performed on the Parks Plateau (Fig. 1). The Blancovin cruise (Figs. 1 and 2) completed the sampling of the Northern Scarp with eleven Alvin upslope dives (acronym BV), mainly located less than 35 km from the Juan de Fuca ridge axis. In addition, eight dredges (acronym BD) sampled the Parks Plateau and an eastern intratransform basin (BD11).

3.2. Textures and mineralogy

The secondary mineralogy of the extrusive unit samples has been detailed in Juteau et al. (1995) and Manac'h et al. (1999). In summary, the lavas are characterized by a low-temperature oxidative alteration (<100 °C), with local development of brown alteration halos in the pillow-lava margins (palagonite, celadonite, smectite, and Fe-oxyhydroxides).

In the lavas, the groundmass texture shows a progressive evolution over less than 5 cm from fresh or palagonitized glassy margins to microlitic cores. The transition zones display spherulitic/variolitic texture characterized by fan-like arrangement of thin plagioclase and fibrous clinopyroxene crystals, enclosing small granular clinopyroxenes or olivines. In more crystallized samples, the texture tends to become intergranular.

Sparse autoclastic breccias (hyaloclastites) have been collected. Clasts consist of rounded to angular hyaline/fine-grained basalt fragments (up to 2.5 cm) cemented by a matrix of crushed and altered glass bearing finely broken phenocrysts (mainly plagioclases).

Lavas are slightly vesicular (<8 vol.%). In the outer part of the flows, amygdules are filled from rims to cores

Table 1
Representative microprobe analyses[a] of plagioclase from BV2958 dive samples

Sample	BV2958-2										BV2958-3				BV2958-4			
Crystal[b]	X. A	X. A	X. A	X. A	X. B	X. B	X. B	X. B	X. C	X. C	P. D	P. D	P. E	P. E	P. F	P. F	P. F	P. F
L (μm)[c]	2650	2650	2650	2650	1925	1925	1925	1925	835	835	700	700	1600	1600	1600	1600	1600	1600
D (μm)[c]	139	171	708	1083	133	227	842	1222	1592	2322	3	83	4	40	63	142	312	346
Zone[d]	An-low	Ca-M	Core	Ca-M	Ca-M	An-low	Core	Inner P	Rim	Core	Rim	Core	Rim	Core	Ca-R	Core	Ca-R	Core
SiO_2	49.86	47.77	48.83	47.33	47.60	49.74	48.88	48.09	48.59	46.29	56.76	54.56	57.77	54.06	54.19	55.13	53.27	54.58
TiO_2	0.03	0.04	0.02	0.02	0.01	0.01	0.03	0.05	0.01	0.00	0.09	0.16	0.00	0.00	0.08	0.09	0.14	0.11
Al_2O_3	31.79	33.57	32.43	33.98	33.20	31.97	32.66	32.69	32.84	34.19	26.48	27.91	25.91	28.51	29.01	28.33	29.47	28.17
FeO[e]	0.46	0.53	0.48	0.51	0.53	0.52	0.58	0.33	0.42	0.43	0.84	0.86	0.81	0.80	0.71	0.82	0.84	0.87
MnO	0.00	0.13	0.03	0.06	0.03	0.06	0.00	0.00	0.03	0.03	0.13	0.00	0.00	0.00	0.00	0.05	0.12	0.05
MgO	0.21	0.18	0.17	0.20	0.20	0.22	0.23	0.21	0.19	0.16	0.11	0.13	0.05	0.14	0.17	0.10	0.11	0.15
CaO	15.46	17.47	16.50	17.65	17.17	15.65	16.45	16.77	16.59	18.45	9.79	11.75	8.96	11.99	12.43	11.64	12.64	11.56
Na_2O	3.00	1.94	2.35	1.63	1.95	2.70	2.59	2.05	2.35	1.29	6.06	5.15	6.48	4.64	4.55	5.03	4.52	4.91
K_2O	0.00	0.00	0.05	0.03	0.01	0.04	0.04	0.00	0.01	0.00	0.09	0.06	0.06	0.04	0.01	0.13	0.03	0.06
P_2O_5	0.00	0.00	0.05	0.00	0.00	0.00	0.06	0.05	0.00	0.00	0.02	0.08	0.00	0.05	0.00	0.03	0.00	0.06
Cr_2O_3	0.00	0.00	0.00	0.00	0.07	0.01	0.05	0.00	0.00	0.00	0.00	0.02	0.03	0.00	0.01	0.14	0.00	0.00
SO_2	0.01	0.00	0.00	0.00	0.00	0.01	0.00	0.00	0.03	0.00	0.00	0.04	0.00	0.00	0.00	0.00	0.05	0.03
Total	100.82	101.62	100.90	101.40	100.76	100.92	101.55	100.24	101.06	100.85	100.37	100.73	100.08	100.24	101.17	101.50	101.20	100.55
An (%)	74	83	79	86	83	76	78	82	80	89	47	56	43	59	60	56	61	56

[a] Compositions were determined using a Cameca SX 50 automated electron microprobe (Microsonde Ouest, Brest, France). Analytical conditions were 15 kV accelerating voltage, 15 nA beam current on a Faraday cup, 6 s counting time, and correction by the ZAF method. Concentrations lower than 0.1 wt.% are considered not representative. Chemical distribution maps (Fig. 9) were obtained in plagioclase xenocrysts (sample BV2958-2) by electron microprobe, with a 10 μm electron beam, a 13 μm analysis step, a 15 kV accelerating voltage, and a 60 nA current.

[b] X.=xenocryst, P.=phenocryst. X. and P. are followed by the letter used to identify the crystals in the text and in Fig. 9. Analyzed points are shown in the profiles of Fig. 9.

[c] L.=length of the crystal, D.=distance of the analyzed point from the right crystal edge.

[d] An-low=An-poor zone, Ca-M=calcic mantle, Inner P.=inner part, Ca-R=calcic rim (for the definition of these zones, see text and Fig. 9).

[e] Total Fe calculated as FeO.

with Fe-oxyhydroxydes, celadonite plus smectite, then calcite (Manac'h et al., 1999). Spherical segregation vesicles are common, sometimes surrounded by tangential plagioclase microlites. They are partially (crescent-shape) or totally filled with more or less recrystallized glass.

Most of the intrusive samples, together with some lava flow cores, have a moderately coarse-grained doleritic texture, generally intergranular, more rarely ophitic.

Consistently with descriptions presented by Juteau et al. (1995), Fleutelot (1997), and Naidoo (1998), lavas are aphyric to moderately phyric (phenocrysts <10 vol.%). Only BN22-14 exhibits olivine accumulation (10–15 vol.%). Plagioclase is the dominant phenocrystic phase (<1 mm long) that frequently forms glomerocrysts. They may enclose small inclusions of plagioclase and/or devitrified glass (<150 μm in diameter) in both rims and cores. The phenocryst margins commonly present a slight optical zoning. A few samples (e.g. BV2955-7 and BV2958-2) host plagioclasic coarse-grained xenoliths (~0.5 cm). Olivine phenocrysts, with Cr-spinel inclusions, are less frequent and partially to completely bowlingitized. Sparse clinopyroxene phenocrysts have been observed, independently of the differentiation degree of the lava. In most cases, small laths of plagioclase are present on the margin of clinopyroxene phenocrysts but in a few lavas (e.g. BV2958-3 and -4) plagioclase phenocrysts partially or totally include clinopyroxenes.

3.3. Mineralogical compositions

Plagioclase phenocrysts and xenocrysts range from andesine to anorthite ($37 \le An \le 98$, Table 1). Microlites have compositions ranging from An_{32} to An_{82}. Sparse

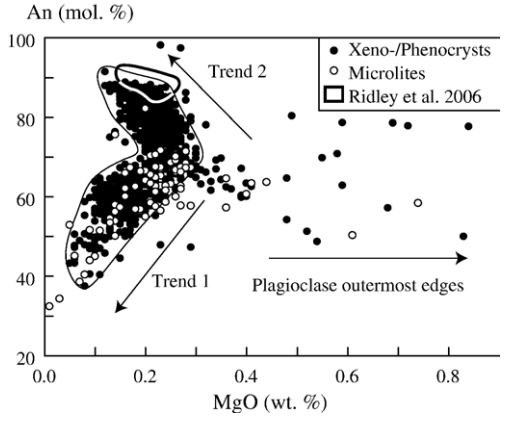


Fig. 3. MgO versus An content in the plagioclases of the Northern Scarp lavas, compared with the plagioclase compositions measured by Ridley et al. (2006) in a cumulate xenolith (EPR, 9°50′N). Selected analyses are given in Table 1.

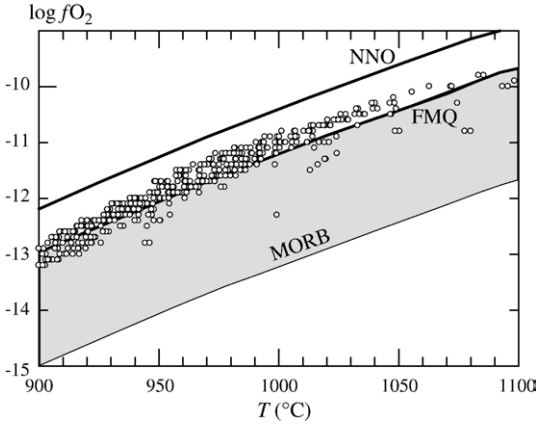


Fig. 4. Plot of log fO_2 versus temperature for coexisting groundmass titanomagnetite-hemoilmenite pairs analyzed in the lava BV2958-3. FMQ: quartz-fayalite-magnetite buffer; NNO: Ni-NiO buffer. MORB field is drawn after Christie et al. (1986) and Lee et al. (2005).

secondary albite has also been identified (pillow-lava BN17-04, hyaloclastite BN18-02). An contents of plagioclase microlites and phenocrysts have been reported versus MgO in the Fig. 3 diagram. Two main trends are identified. Trend 1, including both microlites and phenocrysts, shows a concomitant decrease of MgO and An contents. Trend 2, including mainly phenocrysts plus xenocrysts, is characterized by an increase of An when MgO decreases. The two trends intersect around MgO = 0.25 wt.% and An_{70}. These trends are disturbed by MgO-rich compositions (MgO > 0.3 wt.%), corresponding to the outermost edges of plagioclase phenocrysts.

The olivine phenocrysts range from Fo_{76} to Fo_{85} except the cumulus crystals in the pillow-lava BN22-14 that are more magnesian (Fo_{87-90}). The $^{Fe-Mg}K_D$ values suggest that the olivines with $Fo_{<85}$ have crystallized in equilibrium with the host rock (following Roeder and Emslie, 1970). In BN22-14, the olivine crystals are fresh, euhedral, and do not show any sign of resorption or mechanical stress as expected for peridotite xenocrysts. Consequently, these forsteritic olivines might have crystallized in equilibrium with a not sampled, highly mafic melt (Mg# ~ 74, considering a $^{Fe-Mg}K_D$ value of 0.3).

Clinopyroxene is augitic, except rare pigeonite in the crosscutting dikes BN18-05, -06, and BV2958-2. Their Mg# values ($=100\,Mg/[Mg+Fe^{2+}+Mn]$) range from 64 to 89 in phenocrysts and from 54 to 86 in groundmass crystals.

Groundmass Fe–Ti oxides are mainly granular Ti-magnetite (59 < Usp < 87). Haemoilmenite microlites have also been identified (89 < Ilm < 98) in the sample BV2958-3. The occurrence of coexisting Fe–Ti oxides in this lava allows estimating the oxygen fugacity (fO_2) and crystallization temperature (T). The calculations have

Table 2
Chemical data[a] (wt.% oxide, ppm element) of representative samples from Northern Scarp and Parks Plateau

Location	JdF ridge		NS (west)						
Sample	BN17-02	BN17-11	BN18-01	BN18-03	BN18-07	BV2958-1	BV2958-1s	BV2958-1s	BV2958-2
Reference[b]	1 and 3	1 and 2	3	1	3	1	1	1	1
Type[c]	Basalt	Fe-basalt	Basalt	Basalt	Basalt	Basalt	Seg. Ves.	Seg. Ves.	Diabase
Latitude	44.5	44.5	44.4	44.4	44.4	44.4	44.4	44.4	44.4
Longitude	130.4	130.5	130.2	130.2	130.2	130.2	130.2	130.2	130.2
Depth (m)	−2852	−2174	−3681	−2877	−2501	−2956	−2956	−2956	−2949
Dist. (km)[d]	8.1	3	24.9	26	26.3	27.1	27.1	27.1	27.1
SiO_2	50.50	50.20	49.85	50.50	49.70	50.00	53.00	57.40	49.50
TiO_2	1.55	2.02	1.83	1.70	1.82	1.98	3.97	2.68	1.64
Al_2O_3	14.82	13.87	14.00	14.28	14.30	14.20	12.69	10.51	14.10
Fe_2O_3t[e]	12.13	13.67	12.93	11.55	12.70	12.80	16.26	17.04	12.20
MnO	0.21	0.23	0.22	0.21	0.21	0.20	0.32	0.20	0.20
MgO	7.63	6.91	7.12	7.12	7.06	6.20	1.96	0.44	7.00
CaO	12.15	11.70	11.50	11.70	11.68	11.15	7.68	4.76	11.30
Na_2O	2.38	2.46	2.48	2.56	2.56	2.53	4.03	3.92	2.60
K_2O	0.17	0.20	0.32	0.21	0.20	0.24	0.36	0.78	0.08
P_2O_5	0.17	0.21	0.21	0.16	0.17	0.19	0.64	1.15	0.15
LOI	−0.62	−0.67	−0.11	−0.13	0.10	0.28			0.83
Total	101.09	100.80	100.35	99.86	100.50	99.77	99.31	97.27	99.60
Mg#[f]	60.9	55.6	57.7	60.4	57.9	54.5	25.4	7.3	58.7
Rb	1.7	2.3	3.3	1.2	2.5	3.2	n.d.	n.d.	0.8
Sr	107	104	110	112	105	99	n.d.	n.d.	109
Ba	12	16	18	17	15	22	n.d.	n.d.	13
Sc	43	45	43	45	44	43	n.d.	n.d.	43
V	335	409	360	372	377	403	n.d.	n.d.	350
Cr	288	188	215	158	175	130	n.d.	n.d.	155
Co	45	45	46	47	46	40	n.d.	n.d.	40
Ni	91	63	75	74	71	56	n.d.	n.d.	59
Y	38	48	45	38	41	45	n.d.	n.d.	36
Zr	101	130	129	102	111	117	n.d.	n.d.	94
Nb	2.5	4.0	4.6	3.8	3.6	4.0	n.d.	n.d.	3.5
La	3.9	5.0	5.2	3.9	4.4	4.3	n.d.	n.d.	3.5
Ce	12.0	14.0	16.0	11.3	12.0	12.6	n.d.	n.d.	10.5
Nd	12.0	16.0	16.0	11.2	14.0	12.1	n.d.	n.d.	9.8
Sm	n.d.	n.d.	n.d.	3.5	n.d.	4.3	n.d.	n.d.	3.5
Eu	1.2	1.5	1.6	1.4	1.0	1.5	n.d.	n.d.	1.3
Gd	n.d.	n.d.	n.d.	5.3	n.d.	6.4	n.d.	n.d.	5.0
Dy	6.1	7.7	7.4	6.4	6.9	7.3	n.d.	n.d.	5.9
Er	4.5	5.4	5.2	3.8	4.6	4.5	n.d.	n.d.	3.4
Yb	3.8	4.7	4.5	3.8	4.2	4.5	n.d.	n.d.	3.5
$(La/Yb)_N$[g]	0.7	0.8	0.8	0.7	0.8	0.7			0.7
$(La/Nd)_N$[g]	0.6	0.6	0.6	0.7	0.6	0.7			0.7
$(Dy/Yb)_N$[g]	1.1	1.1	1.1	1.1	1.1	1.1			1.1
$^{87}Sr/^{86}Sr$	0.702488	0.702486		0.702461		0.702440			
$^{143}Nd/^{144}Nd$	0.513173	0.513166		0.513177		0.513197			

(continued on next page)

The full Table 2 is available in the online version of this article; See Appendix A.

[a] Major and trace element analyses were performed by ICP-AES at Brest for whole rocks and by electron microprobe for glass of segregation vesicles (see text). For ICP-AES, the analytical method is described in Cotten et al. (1995). Relative standard deviations are <2% for major elements, Rb and Sr; and <5% for other trace elements. Sr and Nd isotope ratios were measured following the procedure described in Dosso et al. (1991) and using a Thermo-Electron Triton T1 mass spectrometer (UMR6538 "Domaines Océaniques", IUEM, Brest) in dynamic mode for Sr and in static mode for Nd. Sr isotope compositions were corrected for mass fractionation to $^{88}Sr/^{86}Sr = 8.375209$ and normalized to a value of 0.710254 for standard NBS SRM987 ($n = 18$ during the analyses period). Nd isotope compositions were corrected for mass fractionation to $^{146}Nd/^{144}Nd = 0.721903$ and normalized to a value of 0.511866 for standard La Jolla ($n = 14$).

[b] References: 1, this work; 2, Juteau et al. (1995); 3, Fleutelot (1997) and Naidoo (1998).

Table 2 (*continued*)

Location	NS (west)						NS (center)		
Sample	BV2958-3	BV2958-4	BV2958-5	BV2960-2	BV2960-4	BV2960-7	BV2963-9	BN04-09	BN04-12
Reference [b]	1	1	1	1	1	1	1	1 and 3	1
Type [c]	Ni-Fe-bas.	Ni-Fe-bas.	Basalt	Fe-basalt	Basalt	Basalt	Fe-basalt	Fe-basalt	Basalt
Latitude	44.4	44.4	44.4	44.4	44.4	44.4	44.4	44.4	44.4
Longitude	130.2	130.2	130.2	130.1	130.1	130.1	130.0	130.0	130.0
Depth (m)	−2765	−2643	−2549	−3190	−3036	−2492	−2271	−2742	−2291
Dist. (km) [d]	27.3	27.4	27.5	30.8	31	31.4	39.3	40.1	40.1
SiO_2	48.00	49.20	50.20	49.20	49.50	49.50	49.70	49.50	50.20
TiO_2	3.55	3.20	1.81	2.13	1.85	1.36	2.37	2.52	1.98
Al_2O_3	12.55	13.17	14.70	13.50	13.70	15.15	13.80	13.45	13.70
Fe_2O_3t [e]	16.80	15.00	11.75	13.70	13.10	10.80	13.50	14.65	13.05
MnO	0.24	0.23	0.20	0.21	0.20	0.19	0.22	0.23	0.21
MgO	4.98	4.69	6.50	6.20	6.85	8.05	5.60	5.58	6.30
CaO	9.35	9.94	12.00	10.90	11.00	12.00	11.00	10.13	11.40
Na_2O	2.89	2.78	2.57	2.60	2.55	2.30	2.79	2.82	2.63
K_2O	0.22	0.43	0.23	0.20	0.11	0.15	0.32	0.38	0.26
P_2O_5	0.35	0.35	0.17	0.21	0.19	0.14	0.23	0.30	0.19
LOI	0.27	0.38	−0.01	0.93	0.46	−0.15	0.18	0.34	−0.18
Total	99.20	99.37	100.12	99.78	99.51	99.49	99.71	99.90	99.74
Mg# [f]	42.3	43.6	57.8	52.8	56.4	64.9	50.7	48.5	54.4
Rb	2.4	4.8	2.4	2.5	1.2	1.4	3.0	3.1	1.6
Sr	104	104	110	108	108	101	126	131	108
Ba	28	25	17	16	14	11	25	30	15
Sc	44	44	44	46	44	40	46	44	47
V	600	530	390	440	390	305	445	450	408
Cr	110	157	190	66	109	275	94	55	111
Co	48	49	45	49	43	45	44	47	46
Ni	100	116	80	65	52	102	58	40	57
Y	77	75	42	48	42	32	52	57	45
Zr	240	240	113	130	120	76	156	181	121
Nb	8.4	7.6	3.8	4.0	4.6	3.0	6.4	7.3	4.1
La	8.5	8.7	4.6	4.8	4.7	3.1	6.4	8.2	4.3
Ce	25.0	25.8	12.9	14.4	14.2	9.6	18.5	23.0	13.0
Nd	24.0	24.0	12.0	13.6	12.7	8.3	16.5	22.0	12.5
Sm	8.0	7.8	4.3	4.6	4.3	3.1	5.4	n.d.	4.3
Eu	2.5	2.4	1.4	1.7	1.5	1.1	1.8	2.0	1.6
Gd	10.8	10.6	5.6	6.8	5.6	4.3	7.2	n.d.	6.1
Dy	12.7	12.8	6.9	7.7	7.0	5.3	8.6	9.5	7.3
Er	7.8	7.7	4.2	4.8	4.3	3.1	5.2	6.1	4.6
Yb	7.7	7.6	4.1	4.7	4.1	3.1	5.0	5.5	4.4
$(La/Yb)_N$ [g]	0.8	0.8	0.8	0.7	0.8	0.7	0.9	1.1	0.7
$(La/Nd)_N$ [g]	0.7	0.7	0.8	0.7	0.7	0.7	0.8	0.7	0.7
$(Dy/Yb)_N$ [g]	1.1	1.1	1.1	1.1	1.1	1.1	1.2	1.2	1.1
$^{87}Sr/^{86}Sr$	0.702457		0.702490	0.702462	0.702460	0.702479	0.702497	0.702481	0.702453
$^{143}Nd/^{144}Nd$	0.513185		0.513171	0.513184	0.513181	0.513188	0.513169	0.513158	0.513179

[c] Seg. ves.: glass in segregation vesicles; Fe-basalt: ferrobasalt; Fe-diabase: ferrodiabase; Ni-: Ni-rich subaphyric sample; Ol-: sample with olivine accumulation; Hcumulate: heteradcumulate.

[d] Dist.: distance from the Juan de Fuca axis.

[e] Total iron expressed as Fe_2O_3.

[f] Mg# calculated with Fe_2O_3/ Fe_2O_3t ratios from Middlemost (1989).

[g] Chondrite-normalized incompatible trace element ratios (normalization values from Sun and McDonough, 1989).

Table 2 (*continued*)

Location		NS (center)							NS (east)	
Sample	BN23-09	BN02-10	BN02-12	BN06-07	BN06-14	BN10-13	BN10-17	BN01-03	BN22-14	BN22-19
Reference [b]	1	1 and 3	1 and 2	1 and 3	1 and 3	1 and 3	1	1 and 3	2	1 and 3
Type [c]	Basalt	Basalt	Fe-basalt	Basalt	Basalt	Fe-basalt	Basalt	Basalt	Ol-basalt	Fe-basalt
Latitude	44.4	44.4	44.4	44.4	44.4	44.4	44.4	44.4	44.3	44.3
Longitude	130.0	130.0	130.0	130.0	130.0	130.0	129.9	129.9	129.8	129.8
Depth (m)	−3638	−3600	−3409	−3062	−2300	−3457	−2993	−2492	−2613	−2292
Dist. (km) [d]	40.4	40.9	40.9	41.5	41.4	43.2	43.8	44.3	52.3	53.3
SiO_2	49.30	48.90	48.85	49.80	50.20	47.60	49.20	50.70	45.00	49.80
TiO_2	1.18	1.06	3.61	1.66	1.65	2.34	1.68	2.38	1.36	2.42
Al_2O_3	15.00	15.58	11.62	14.30	14.54	13.54	14.10	14.60	13.70	13.25
Fe_2O_3t [e]	9.74	9.59	19.10	12.30	11.80	14.10	12.00	12.73	10.23	14.55
MnO	0.19	0.16	0.26	0.20	0.20	0.21	0.21	0.21	0.20	0.23
MgO	7.80	8.15	4.27	7.20	7.32	6.25	7.43	5.14	15.00	6.05
CaO	11.45	11.87	7.78	11.73	11.85	10.00	11.70	11.49	9.30	10.98
Na_2O	2.86	2.27	3.10	2.51	2.56	2.97	2.46	2.69	2.47	2.54
K_2O	0.10	0.13	0.34	0.15	0.21	0.10	0.12	0.38	0.05	0.35
P_2O_5	0.11	0.12	0.52	0.17	0.17	0.28	0.17	0.26	0.12	0.26
LOI	1.81	2.38	1.08	−0.35	−0.26	2.50	0.77	0.10	2.31	−0.04
Total	99.54	100.21	100.53	99.67	100.24	99.89	99.90	100.68	99.75	100.39
Mg# [f]	66.5	67.8	35.6	59.2	60.6	52.3	60.5	50	78.4	50.7
Rb	0.3	2.5	4.7	1.7	2.0	1.1	0.5	4.4	0.6	4.7
Sr	116	117	115	101	104	108	119	117	250	108
Ba	21	12	38	12	13	11	12	23	3	21
Sc	43	39	40	44	44	45	45	46	31	44
V	282	157	410	356	345	418	365	445	185	460
Cr	304	272	8	206	200	122	280	105	460	120
Co	44	44	46	43	43	44	44	46	64	44
Ni	77	108	15	69	71	48	75	49	580	50
Y	27	24	100	38	38	62	37	53	27	54
Zr	69	64	332	99	100	190	112	155	115	165
Nb	2.9	2.5	12.0	3.2	2.8	5.6	4.3	5.3	1.2	4.5
La	2.7	3.2	13.3	3.7	4.0	6.9	4.4	6.0	3.8	6.0
Ce	6.4	9.5	42.0	12.5	12.0	21.0	13.0	18.5	13.0	17.5
Nd	7.7	10.0	40.0	12.0	11.5	22.0	11.4	18.0	10.5	19.0
Sm	2.5	n.d.	n.d.	n.d.	n.d.	n.d.	3.70	n.d.	n.d.	n.d.
Eu	1.1	0.95	3.3	1.4	1.3	2.1	1.4	2.0	1.2	1.4
Gd	3.5	n.d.	n.d.	n.d.	n.d.	n.d.	5.1	n.d.	n.d.	n.d.
Dy	4.5	3.9	16.2	6.1	6.3	9.9	6.2	8.7	4.2	9.2
Er	2.6	2.6	10.7	4.1	3.9	6.3	3.6	5.7	2.8	6.1
Yb	2.6	2.3	9.7	3.7	3.7	6.1	3.7	5.2	2.5	5.5
$(La/Yb)_N$ [g]	0.8	1.0	1.0	0.7	0.8	0.8	0.9	0.8	1.1	0.8
$(La/Nd)_N$ [g]	0.7	0.6	0.7	0.6	0.7	0.6	0.8	0.7	0.7	0.6
$(Dy/Yb)_N$ [g]	1.2	1.1	1.1	1.1	1.2	1.1	1.1	1.1	1.1	1.1
$^{87}Sr/^{86}Sr$	0.702304	0.702281	0.702445	0.702430	0.702469	0.702413	0.702510	0.702494		0.702482
$^{143}Nd/^{144}Nd$	0.513287	0.513288	0.513172	0.513175	0.513175	0.513188	0.513156	0.513167		0.513181

(continued on next page)

been made from the compositions of mineral pairs, using the ILMAT program of Lepage (2003) and the thermo-barometer equations of Andersen and Lindsley (1985). Calculated temperatures vary from 760 °C to 1398 °C. Only Fe–Ti oxides equilibrated at $900 < T < 1100$ °C have been considered to constrain the magmatic fO_2 values. Results, shown in Fig. 4, yield to fO_2 values plotting between the FMQ and NNO buffers.

4. Geochemistry of the WBD samples

4.1. Methods

31 samples of the lava unit from the Northern Scarp (lavas and crosscutting dikes), with loss on ignition (LOI) lower than 3 wt.%, were selected for chemical analyses (Table 2) to complete the available WBD data of Juteau

Table 2 (*continued*)

Location	PP (west)	PP (center)		PP (east)					Intratransform basin
Sample	BD01-02C	BD04-01A	BN14-07	BD05-21A	BD08-01E	BD08-02	BD08-04B	BD08-05	BD11-01
Reference[b]	1 and 3	1 and 3	2	1 and 3	3	3	1 and 3	3	1 and 3
Type[c]	Basalt	Basalt	Ol-basalt	Ol-basalt	Ni-Fe-bas.	Ni-basalt	Ni-basalt	Ni-basalt	Ni-basalt
Latitude	44.4	44.3	44.3	44.2	44.3	44.3	44.3	44.3	44.2
Longitude	130.2	130.2	130.1	129.7	130.0	130.0	130.0	130.0	129.5
Depth (m)	−2850	−2530	−3561	−2650	−2000	−2000	−2000	−2000	−3287.5
Dist. (km)[d]	3	32	35.4	54	42	42	42	42	72
SiO_2	49.20	49.60	47.90	47.75	48.85	48.40	49.00	49.00	50.00
TiO_2	1.43	1.63	1.54	1.14	2.65	2.22	2.41	2.40	1.85
Al_2O_3	17.10	15.80	15.20	15.74	14.20	15.30	14.75	14.60	14.50
Fe_2O_3t[e]	9.87	11.25	10.40	11.08	14.25	11.60	12.60	12.52	12.40
MnO	0.16	0.27	0.16	0.18	0.23	0.16	0.26	0.28	0.20
MgO	6.08	7.14	10.20	10.45	6.70	5.60	7.00	7.00	8.08
CaO	12.05	11.30	10.80	10.45	9.50	9.70	9.05	8.92	10.00
Na_2O	2.66	2.73	2.65	2.45	3.10	3.20	3.40	3.50	2.80
K_2O	0.15	0.22	0.26	0.27	0.37	1.41	0.88	0.88	0.21
P_2O_5	0.17	0.20	0.17	0.13	0.35	0.40	0.44	0.44	0.22
LOI	1.20	−0.53	0.80	0.36	−0.59	2.23	0.28	−0.04	−0.55
Total	100.07	99.61	100.08	100.00	99.61	100.28	100.07	99.50	99.71
Mg#[f]	60.4	61.1	70.8	70	53.8	54.4	57.9	58.1	61.7
Rb	2.0	2.8	2.7	4.5	4.8	25.0	12.5	12.5	3.1
Sr	158	155	165	140	165	357	270	270	140
Ba	20	30	18	12	44	148	127	156	30
Sc	39	40	36	37	37	32	34	34	36
V	272	295	270	205	345	270	300	300	285
Cr	187	218	450	375	190	237	225	225	295
Co	39	45	58	53	43	41	43	43	44
Ni	50	79	330	272	94	128	112	120	148
Y	29	32	32	24	53	40	47	46	36
Zr	96	112	108	74	208	205	220	225	125
Nb	4.5	5.7	4.3	3.3	11.7	21.4	21.5	21.4	6.8
La	4.6	5.5	4.7	3.4	10.5	16.6	16.3	16.4	6.1
Ce	13.0	15.0	13.0	9.0	28.0	36.0	37.0	36.0	16.0
Nd	10.5	12.5	11.5	8.0	22.0	23.0	23.5	24.0	13.0
Sm	n.d.	n.d.	n.d.	n.d.	n.d.	n.d.	n.d.	n.d.	n.d.
Eu	1.2	1.3	1.4	1.0	2.1	1.8	2.0	1.9	1.5
Gd	n.d.	n.d.	n.d.	n.d.	n.d.	n.d.	n.d.	n.d.	n.d.
Dy	5.0	5.6	5.0	4.3	9.0	6.8	8.0	8.0	6.1
Er	2.9	3.3	3.0	2.5	5.3	3.9	4.6	4.6	3.6
Yb	2.8	3.2	2.9	2.6	5.1	3.8	4.6	4.5	3.5
$(La/Yb)_N$[g]	1.2	1.2	1.2	1.0	1.5	3.1	2.6	2.6	1.3
$(La/Nd)_N$[g]	0.9	0.9	0.8	0.8	0.9	1.4	1.4	1.3	0.9
$(Dy/Yb)_N$[g]	1.2	1.2	1.2	1.1	1.2	1.2	1.2	1.2	1.2
$^{87}Sr/^{86}Sr$	0.702356	0.702347		0.702451			0.702700		0.702367
$^{143}Nd/^{144}Nd$	0.513227	0.513227		0.513208			0.513182		0.513245

et al. (1995), Fleutelot (1997), and Naidoo (1998). Major and trace elements were measured at Brest University on whole rock powders by inductively coupled plasma atomic emission spectrometer (ICP-AES). Some Blancovin analyses (DCP and ICP spectrometries) on different powders have already been presented in Pollock et al. (2005). Concentrations diverge from our analyses up to 130 relative percent (for Ni in BV2958-1, in which Pollock et al. (2005) reported excess olivine, contrary to us). Consequently, we repeated the concentration determination on new powders, using both ICP-AES and ICP-MS, for the five samples of the dive BV2958 (Table 3). Differences between our triplicates are minor, except for the mobile elements K_2O, Rb, and Ba. To avoid introducing an analytical bias in our interpretations, we choose in this instance to use only chemical data obtained by ICP-AES. In samples BV2958-1 and BV2963-8, glass of segregation vesicles was analyzed for major elements by electron microprobe (Table 2).

Sr and Nd isotope ratio determination of twenty-six samples from the Northern Scarp and Parks Plateau were performed (Table 2). In order to remove seawater alteration effects, the whole-rock powders were leached with 2.5 N HCl for one hour and rinsed in ultrapure water three times. Sample BD08-04B, clearly shifted toward high $^{87}Sr/^{86}Sr$ values, was subjected to a more aggressive leaching in 6 N HCl during one hour. However, the 6 N HCl leached composition does not significantly differ from that leached with 2.5 N HCl.

4.2. Loss on ignition, major and compatible trace elements

In each dive, LOI values tend to increase with depth. No clear correlation between LOI and major elements concentrations has been observed for the whole dataset (e.g. K_2O versus LOI, Fig. 5a).

All the WBD lavas and crosscutting dikes are basalts, except the basaltic andesite BN13-08 (total alkali-silica diagram of Le Bas et al., 1986). Their compositions range from mafic terms to ferrobasalts ($FeO^t > 12$ wt.% and $TiO_2 > 2$ wt.%, Byerly, 1980). The Northern Scarp samples display the most differentiated compositions. The major element variations in segregation vesicle glasses of BV2958-1 and BV2963-8 (Northern Scarp) are studied together with the whole rock analyses on the Fig. 5 diagrams. Even if such compositions are the result of local post-emplacement *in situ* crystallization, they can be used as rough equivalents of the products of magma chamber differentiation. They range from basaltic to dacitic and tend toward the composition of a dacite collected on the Cleft segment (Stakes et al., 2006). In major elements versus MgO diagrams (Fig. 5b and d), compositions of samples and segregation vesicles display the typical crystallization trends of tholeiites: TiO_2 and $Fe_2O_3^t$ increase when MgO decreases (from 9 to ~3 wt.%, Fig. 5b), then decrease in segregation vesicles; CaO and Al_2O_3 decrease (Fig. 5c), and Na_2O, K_2O and P_2O_5 increase continuously (Fig. 5d). While the Northern Scarp and Parks Plateau variation trends appear largely similar, the Parks Plateau data are more widely scattered and do not fall along a well-defined crystallization trend like the Northern Scarp samples. In addition, the Parks Plateau lavas are characterized by the highest Al_2O_3 values and sometimes by lower TiO_2 contents. Three samples show evidence for olivine accumulation (MgO > 10 wt.%). Finally, some non-cumulative samples from both the Northern Scarp and Parks Plateau (including three samples of the BD08 dredge) fall to the right of the main trend in the TiO_2 and P_2O_5 versus MgO diagrams (Fig. 5b and d).

Differentiation results in a decrease of the compatible trace element contents when La, taken here as the reference highly incompatible element, increases (Ni in Fig. 5e and Cr not shown). The olivine-cumulative samples are shifted toward high Ni concentrations (>250 ppm). However, crystallization and accumulation cannot explain the extent of the observed variations. Even if poor in olivine phenocrysts, the samples shifting apart in the TiO_2 and P_2O_5 diagrams also fall clearly above the main trend in the Ni versus La diagram (Fig. 5e). This is also true for Cr (Table 2). Two of these Ni-rich samples have been triplicated and the shift in compatible elements is still observed, regardless of the powder and the analytical method (Table 3).

4.3. Incompatible trace elements and Sr–Nd isotopes

As it is difficult to clearly distinguish samples from the Northern Scarp and Parks Plateau with major elements and Ni, moderately to highly incompatible trace elements can be used to discriminate lavas from both sites. First, Sr is systematically lower in the Northern Scarp (Sr < 130 ppm, except BN22-14) than in the Parks Plateau lavas (Table 2). Low-temperature reactions with seawater cannot account for such a geographical distribution of Sr as alteration does not differ between both flanks. Moreover, in incompatible trace element versus La diagrams (Fig. 5f–h), the Northern Scarp and Parks Plateau basalts define two linear contrasted trends. The Northern Scarp samples, which display the lowest Nb/La (Nb/La = 0.9 ± 0.2), La/Nd ($La/Nd_N = 0.7 \pm 0.1$), and La/Yb ratios ($La/Yb_N = 0.7 \pm 0.6$), somehow mimic the Cleft variations in the Yb–La diagram (Fig. 5h). These features characterize normal MORBs (N-MORBs). In this way, the normalized rare earth element (REE) patterns of the Northern Scarp lavas are grossly parallel, depleted in LREE and flat between MREE and HREE (Fig. 6a). Consistently with the effects of fractional crystallization, the less mafic samples are characterized by higher abundances in REE and also the development of a slight negative Eu anomaly (e.g. dive BV2958, Fig. 6a). Three out of four Ni-rich samples of the dredge BD08 from the Parks Plateau (except BD08-01) shift apart from the variation trends of the Plateau due to their very high La and Nb and low Nd and Yb contents (Fig. 5f–h). Such features resemble those of one Gorda sample (Davis et al., 1998, Fig. 5g–h). The REE patterns of the BD08 basalts also have the steepest slopes in chondrite normalized diagrams, characteristic of enriched MORBs ($La/Yb_N = 2.8 \pm 0.6$ and $Dy/Yb_N = 1.2 \pm 0.1$, Fig. 6b).

Sr–Nd isotope ratios of the WDB samples are shown in the $^{143}Nd/^{144}Nd$ versus $^{87}Sr/^{86}Sr$ diagram of Fig. 7,

Table 3
Comparison of composition of samples from dive BV2958 determined using different analytical methods

Sample	2958-1	2958-1	2958-1	2958-1	2958-2	2958-2	2958-2	2958-2	2958-3	2958-3	2958-3	2958-3	2958-5	2958-5	2958-5	2958-5
Method [a]	AES	AES*	MS	Pollock	AES	AES*	MS	Pollock	AES	AES*	MS	Pollock	AES	AES*	MS	Pollock.
SiO_2	50.00	49.70		*49.51*	49.50	49.80		*49.87*	48.00	48.20		*50.03*	50.20	50.20		*50.86*
TiO_2	1.98	2.00		*2.43*	1.64	1.66		*2.94*	3.55	3.65		*2.16*	1.81	1.81		*2.00*
Al_2O_3	14.20	14.45		*13.20*	14.10	14.30		*13.09*	12.55	12.53		*13.58*	14.70	14.80		*14.04*
Fe_2O_3t [b]	12.80	12.80		*14.58*	12.20	12.16		*15.63*	16.80	17.00		*13.31*	11.75	11.55		*12.07*
MnO	0.20	0.21		*0.21*	0.20	0.19		*0.21*	0.24	0.25		*0.22*	0.20	0.20		*0.20*
MgO	6.20	6.20		*6.67*	7.00	7.11		*5.79*	4.98	5.04		*6.47*	6.50	6.60		*6.48*
CaO	11.15	11.25		*10.53*	11.30	11.60		*9.82*	9.35	9.40		*11.33*	12.00	11.75		*11.22*
Na_2O	2.53	2.57		*2.61*	2.60	2.57		*2.76*	2.89	2.90		*2.83*	2.57	2.55		*2.72*
K_2O	0.24	0.20		*0.28*	0.08	0.10		*0.17*	0.22	0.23		*0.21*	0.23	0.24		*0.26*
P_2O_5	0.19	0.19		n.d.	0.15	0.15		n.d.	0.35	0.36		n.d.	0.17	0.16		n.d.
LOI	0.28	0.20		*0.50*	0.83	0.42		*0.70*	0.27	0.06		*0.20*	−0.01	−0.07		*0.70*
Total	99.77	99.77		*100.02*	99.60	100.06		*100.29*	99.20	99.62		100.14	100.12	99.79		*99.87*
Rb	3.2	n.d.	1.5	2.8	0.8	n.d.	0.6	0.7	2.4	n.d.	1.8	1.8	2.4	n.d.	2.1	2.6
Sr	99	102	104	*112*	109	110	111	*106*	104	105	105	*108*	110	110	111	*113*
Ba	22	50	49	20	13	15	14	11	28	30	29	25	17	19	18	16
Sc	43	45	46.6	*44.0*	43	45	46.9	*46.3*	44	46	48.2	*44.5*	44	45	46.6	*45.6*
V	403	415	402	*405*	350	364	356	*343*	600	630	639	*506*	390	385	385	*383*
Cr	130	132	125	144	155	165	156	183	110	111	105	146	190	185	179	193
Co	40	49	48	52	40	45	45	42	48	56	56	48	45	42	44	42
Ni	56	75	75	129	59	64	63	87	100	109	105	98	80	72	69	92
Y	45	46	49.6	46.0	36	38	39.7	34.0	77	79	86.3	75.0	42	42	44.8	42.0
Zr	117	125	131	122	94	100	105	97	240	245	264	220	113	115	119	121
Nb	4.0	4.5	4.1	3.9	3.5	3.9	4.0	3.1	8.4	8.5	8.6	7.0	3.8	4.1	4.5	4.1
La	4.3	4.7	4.4	4.0	3.5	4.1	3.8	3.1	8.5	9.2	8.9	7.5	4.6	4.5	4.4	4.2
Ce	12.6	13.5	13.5	12.6	10.5	11.4	11.3	9.8	25.0	26.5	26.6	23.0	12.9	13.5	13.0	13.0
Nd	12.1	13.0	12.9	12.1	9.8	11.0	10.7	9.3	24.0	25.0	24.7	22.0	12.0	12.0	12.1	12.2
Sm	4.3	4.5	4.55	4.29	3.5	3.7	3.75	3.22	8.0	8.2	8.37	7.47	4.3	4.1	4.21	4.16
Eu	1.5	1.6	1.56	1.38	1.3	1.3	1.36	1.13	2.5	2.5	2.58	2.21	1.4	1.4	1.49	1.41
Gd	6.4	6.6	6.23	6.21	5.0	5.1	5.07	4.84	10.8	11.0	11.01	10.59	5.6	5.6	5.61	6.00
Dy	7.4	7.6	7.74	7.07	5.9	6.2	6.32	5.63	12.7	13.0	13.51	12.17	6.9	6.7	7.09	6.97
Er	4.5	4.6	4.92	4.46	3.4	3.8	3.99	3.41	7.8	8.0	8.63	7.26	4.2	4.2	4.48	4.33
Yb	4.5	4.7	4.55	4.32	3.5	3.8	3.70	3.20	7.7	7.9	8.07	6.94	4.1	4.2	4.24	3.98

[a] AES: ICP-AES analyses (Brest); AES*: ICP-AES re-analyses on a new powder (Brest); MS: ICP-MS re-analyses on the same powder than AES*; Pollock: analyses of Pollock et al. (2005) by DCP (elements marked in italic) and by ICP-MS (other elements). Our ICP-MS analyses were conducted using a procedure modified after Barrat et al. (1996), on a Thermo-Finnigan Element 2. The external standard used to calculate element concentration is the U.S. Geological Survey standard BHVO-2. BIR-1 and PMS were standards used to check the validity of the method.

[b] Total iron expressed as Fe_2O_3.

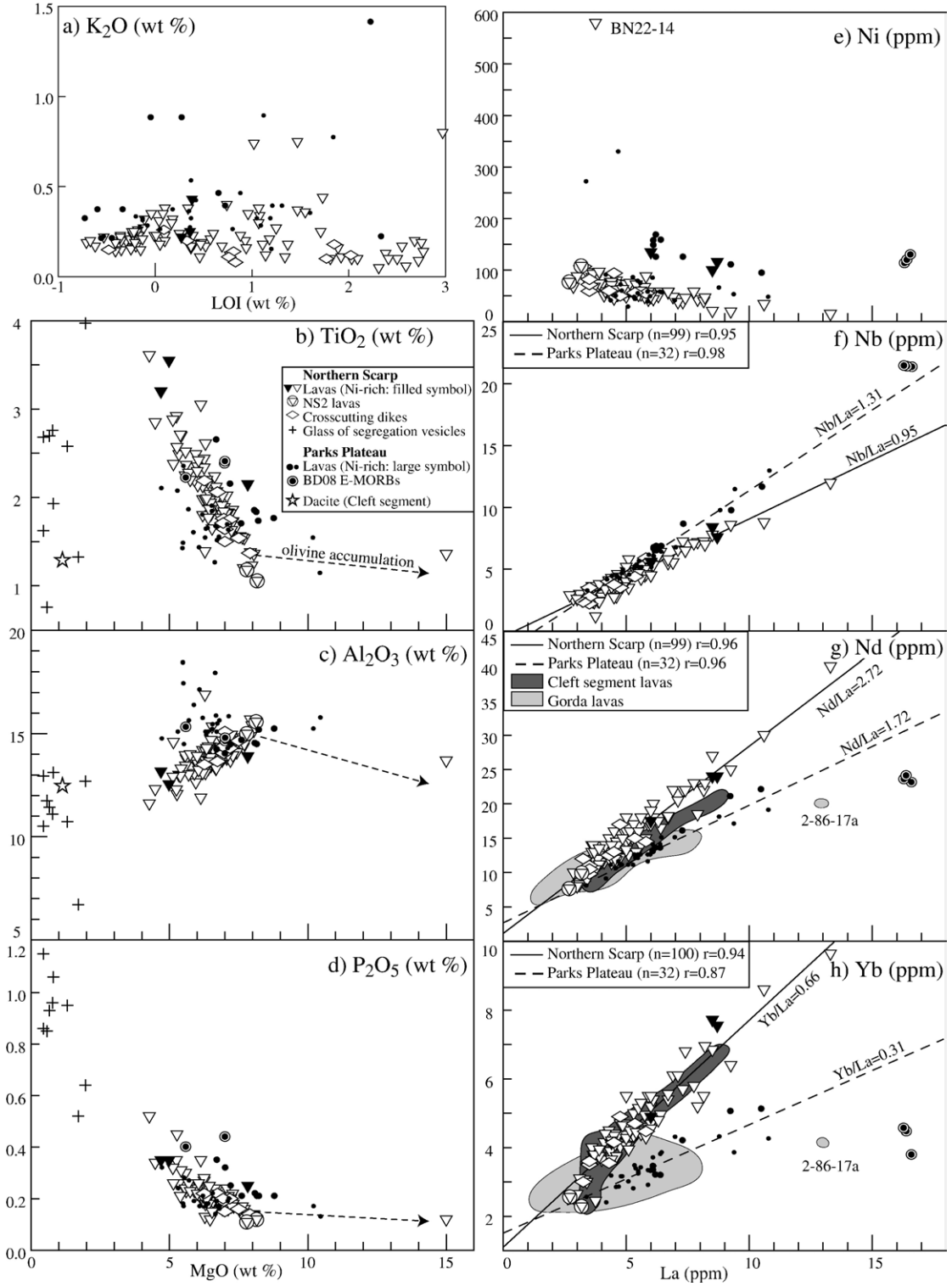


Fig. 5. a) K_2O versus LOI variations for relatively fresh Northern Scarp and Parks Plateau lavas and crosscutting dikes (LOI < 3 wt.%). b–h) Selected major oxide (wt.%) and trace element (ppm) variation diagrams versus MgO and La, respectively. The major element composition of the RC10 dacite collected on the Cleft segment is shown for comparison (Stakes et al., 2006). The dashed arrows illustrate the chemical effects induced by olivine accumulation. Linear regressions in incompatible trace element diagrams are shown for both the Northern Scarp and Parks Plateau (except BD08) samples. Cleft field: Smith et al. (1994); Rhodes et al. (1990). Gorda field and sample 2-86-17A: Davis and Clague (1987); Davis et al. (1998).

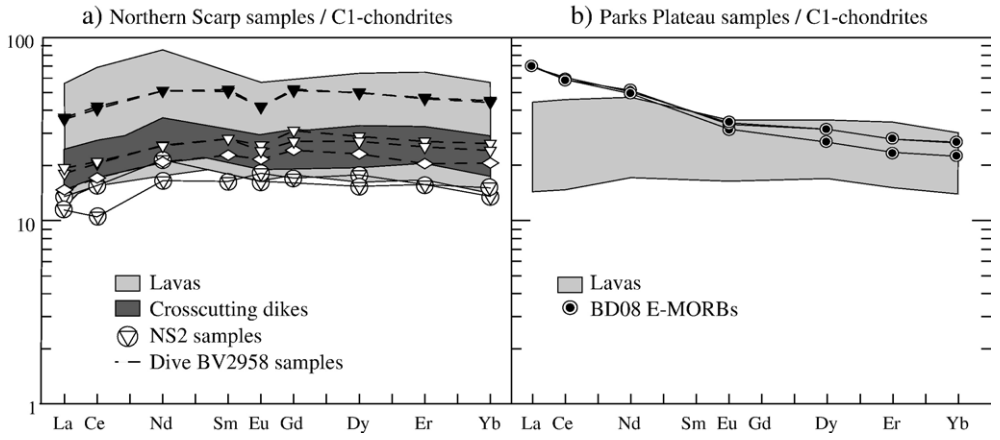


Fig. 6. Fields for C1-chondrite-normalized REE patterns for a) the Northern Scarp samples and b) the Parks Plateau samples (normalization values from Sun and McDonough, 1989). Patterns of representative samples of the dive BV2958 (Northern Scarp) are shown. The NS2 (defined from isotopic features) and BD08 samples are also plotted. Symbols as in Fig. 5.

together with fields for the lavas from the Juan de Fuca Ridge, including the Cleft segment, and the Gorda ridge. Data from the WBD define an array with a negative slope.

Most of the Northern Scarp lavas (18 N-MORBs, NS1) have homogeneous isotope compositions. NS1 samples have the lowest $^{143}Nd/^{144}Nd$ of the WBD dataset (≤ 0.513172), comparable to those measured in the Cleft Segment lavas. Two Northern Scarp basalts (BN02-10 and BN23-09, NS2), collected at the sheeted-dike complex/extrusive boundary, shift toward high $^{143}Nd/^{144}Nd$ values (>0.513250), above the Juan de Fuca field. The four Parks Plateau basalts (PP) plot between NS1 and NS2 ($0.513208 \leq {}^{143}Nd/^{144}Nd \leq 0.513245$), except the enriched MORB BD08-04B, which is characterized by an elevated $^{87}Sr/^{86}Sr$ ratio. This sample plots outside the Juan de Fuca field but inside the Gorda one. All BD08 samples should share this isotopic signature except for BD08-01E which appears to have different trace element ratios, similar to those of other Parks Plateau samples.

Isotope and trace element data can be used to distinguish the samples with respect to the geographic area (NS/PP) or their specific location in the lithological succession (NS1 within the extrusive unit and NS2 at the sheeted-dike/extrusive transition). The distribution of the Northern Scarp samples in the Sr–Nd diagram (Fig. 7) is consistent with a binary mixing between a Cleft-type mantle component and a depleted NS2-type mantle source. Such a highly depleted isotopic composition is not observed elsewhere in the Pacific, except in the western rift of the Easter Microplate, the Lamont seamounts, and the Garrett Transform Zone (Wendt et al., 1999; our unpublished data). It might be considered representative of a nearly pure depleted end-member and interpreted as the residue of a previous low-extent mantle melting event (Wendt et al., 1999).

The geochemical characteristics of the Parks Plateau lavas do not help to decipher the plateau origin (seamount versus accretion at the Cleft segment tip). Most of the PP samples fall within the Juan de Fuca field but BD08-04B plots within the Gorda isotope field (Fig. 7) and presents trace element features similar to Gorda MORBs (Fig. 5g–h). However, discussing the geodynamic signification of the Parks Plateau is out of scope

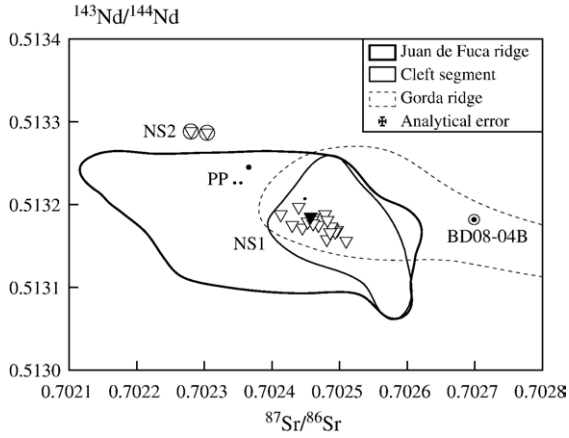


Fig. 7. $^{143}Nd/^{144}Nd$ versus $^{87}Sr/^{86}Sr$ diagram showing the isotope ratios of the Northern Scarp and Parks Plateau samples, compared with the lavas of the Juan de Fuca and Gorda ridges. Juan de Fuca and Cleft segment fields: Cohen et al. (1980); Hegner and Tatsumoto (1987); Ito et al. (1987); White et al. (1987); Rhodes et al. (1990); Cousens et al. (1995); Chadwick et al. (2005). Gorda field: White et al. (1987); Goldstein et al. (1991); Volpe and Goldstein (1993); Davis et al. (1998). Symbols as in Fig. 5.

of this study and additional data would be required before drawing any general conclusion.

5. Identification of the main magmatic processes operating in the Northern Scarp magma reservoir

Given the relative constancy of incompatible trace element and isotope ratios within the NS1 group (Figs. 5 and 7), the corresponding lavas can be regarded as issued from a quite homogeneous mantle source under steady melting conditions. The trends identified in the major element diagrams of Fig. 5 imply that fractionation of olivine, plagioclase, and augite has played a major role in the differentiation of NS1 samples. The sharp decrease of TiO_2 in the segregation vesicles and Cleft dacite shows evidence for the crystallization of Fe–Ti oxides around MgO = 2–4 wt.%. The fact that the NS2 and Parks Plateau samples distribute in the same trends as NS1 in all major and compatible trace element diagrams (Fig. 5b–e) suggests that the corresponding contrasted primary melts have recorded roughly comparable differentiation processes. In particular, subaphyric Ni-rich samples have been collected on both sites. Their anomalously high Ni and MgO values are consistent neither with mineral accumulation, nor with fractional crystallization, nor with source heterogeneity, as the isotopic ratios of the corresponding samples are not distinguishable from the other WBD samples (Fig. 7). Such chemical features might have been acquired during equivalent petrogenetic processes in both magmatic systems. The Ni-rich samples distribute roughly along straight lines in the TiO_2 and P_2O_5 versus MgO and Ni versus La diagrams of Fig. 5b and d–e. Linear chemical variations, together with the fact that a few Ni-rich lavas are ferrobasalts, suggest a binary mixing process between felsic and mafic end-members.

To extend the WBD Ni–Mg# correlation toward mafic terms in the Fig. 8 diagram (leaving the Ni-rich samples apart), we made the assumption that olivine is the main liquidus phase that controls the concentrations of these two elements in melts with Mg# > 65. Concomitant plagioclase crystallization would have no effect on MgO, FeO, and Ni. Equilibrium olivine was added to the most mafic, fresh and subaphyric sample BV2960-7 (Mg# = 64.9), with an increment of 1% and assuming Rayleigh fractionation, until reproducing a composition close to that of the olivine-cumulative lava BN22-14 (Fig. 8). We adjusted the MgO content in olivine at each step by considering a $^{Fe-Mg}K_D$ value of 0.3 (Roeder and

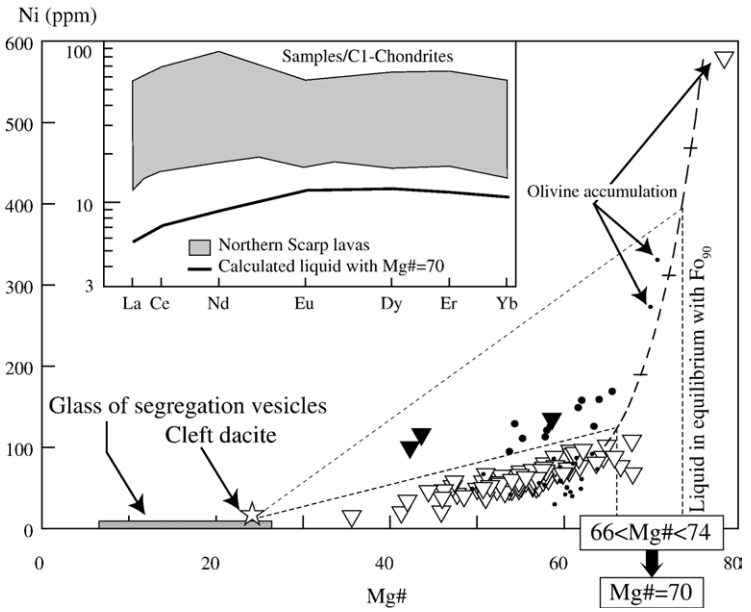


Fig. 8. Ni (ppm) versus Mg# diagram for the Northern Scarp and Parks Plateau lavas. The dashed curve is the mafic extension of the Ni–Mg# hyperbolic correlation, calculated from the most mafic, fresh, and subaphyric sample BV2960-7 (see text for the method). Dark gray field indicates the Mg# composition of the glass of segregation vesicles. The Cleft segment dacite (Stakes et al., 2006) is used to approach the felsic end-member in the mixing model. The supposed mixing field is bounded by dashed lines and is used to propose a mean Mg# and REE composition of the mafic end-member (see text for further explanation). Inset: REE pattern of the calculated refilling melt together with field of the Northern Scarp lavas, NS2 samples not included (Sun and McDonough, 1989). Symbols as in Fig. 5.

Emslie, 1970) and we considered a partition coefficient of Ni in olivine directly related to the liquid composition ($d^{Ni}=(124.13/MgO_{liq})-0.897$, Hart and Davis, 1978).

6. The dive BV2958: petrologic investigation of crystallization under hydrous conditions coupled with magma mixing

6.1. The dive BV2958

The dive BV2958, located 27 km east of the axis (Fig. 2), was chosen for a detailed petrologic study owing to several reasons. (i) The collected samples cover a significant range of time, since the vertical stratigraphy overlaps three magnetic periods (from Brunhes to Jaramillo, Fig. 2). (ii) The samples present remarkable petrographic features: both types of including relations between plagioclase and clinopyroxene phenocrysts are observed, and the dike BV2958-2 contains one coarse-grained xenolith (0.6*0.5 cm) made up of highly zoned plagioclases, bearing recrystallized glass inclusions (Fig. 9b and d, inset). (iii) From a chemical point of view, the samples collected during this dive are fresh (LOI<1 wt.%) and show a large range of whole rock compositions, from quite mafic (Mg#=58.7, BV2958-2) to ferrobasaltic (Mg#>42.3, BV2958-3 and -4, Table 2). This compositional range is extended by the glass compositions of segregation vesicles in sample BV2958-1. In addition, two olivine-poor, Ni-rich lavas (BV2958-3 and -4), interpreted as mixing products, occur just below the Bruhnes/Matuyama isochrone.

6.2. Plagioclase as a marker of magmatic processes

Plagioclase, one of the commonest igneous minerals, has been extensively studied to return to magma chamber evolution and dynamics during the crystal growth because it shows more pronounced chemical zoning than any other mineral group. Changes in the major element composition of plagioclase are controlled by a large number of chemical and physical parameters (mainly melt composition, volatile content, and temperature, Smith and Brown, 1988).

Chemical traverses have been made in the plagioclase xenolith of the dike BV2958-2 and in phenocrysts of the overlying lavas BV2958-3 and -4. Representative analyses of the profiles are shown in Table 1. The chemical profiles are plotted in An versus MgO diagrams (Fig. 9) in order to set their compositions back in the two trends previously defined by using the whole plagioclase dataset (Fig. 3). These profiles are also compared to the compositions of theoretical plagioclases crystallizing in equilibrium with the host rocks (BV2958-2,-3, and -4, see calculation method in Fig. 9).

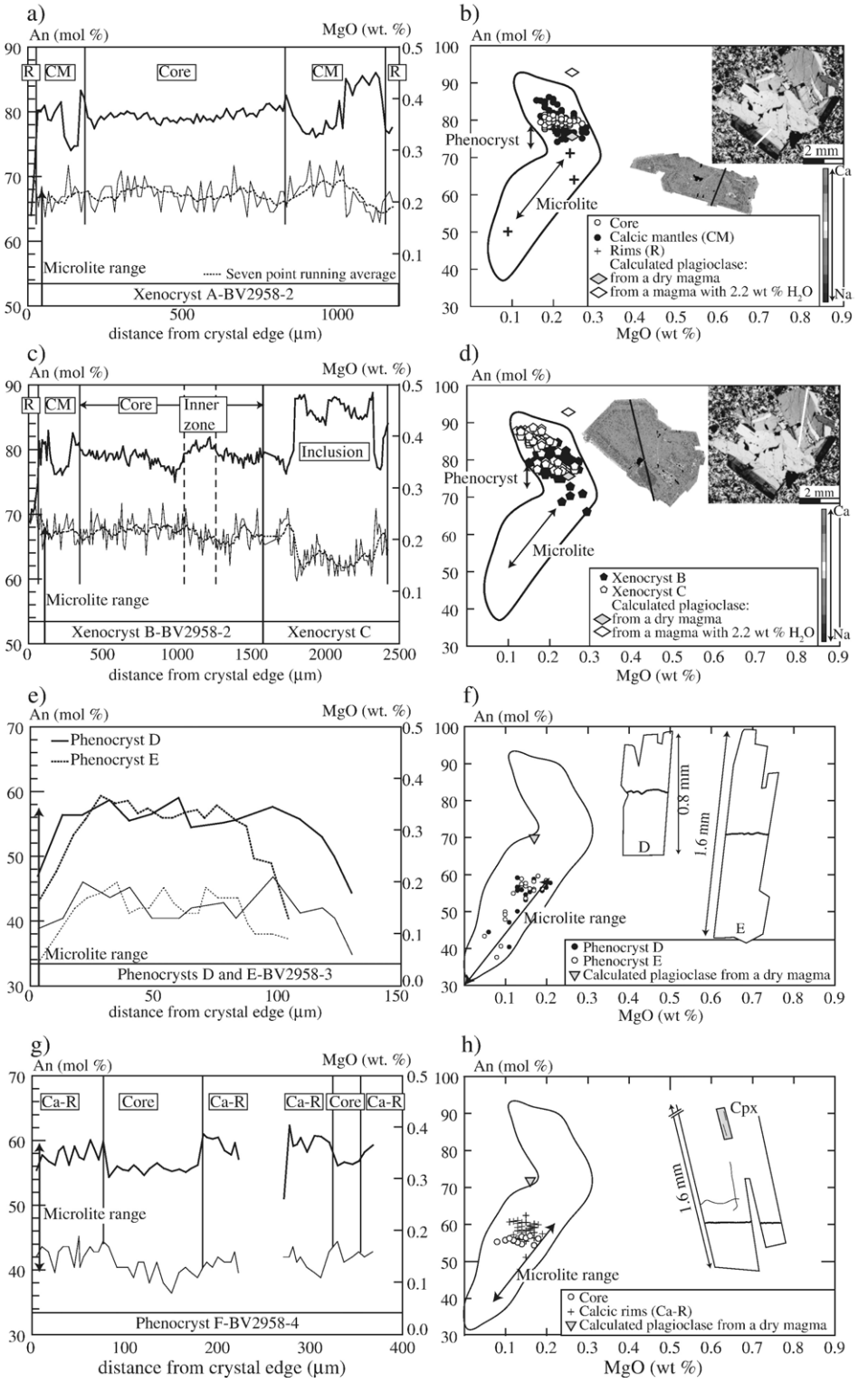
The outermost edges of plagioclase crystals are characterized by a MgO increase without any change in the An content (Fig. 3, not shown in Fig. 9), which probably records local kinetic effects. After lava eruption, the crystal growth rates are higher than the rates of element diffusion through the melt and it leads to the formation of a chemical boundary layer at the crystal-melt interface. So as not to take into account these chemical effects, analyses with MgO>0.3 wt.% will not be considered further.

The concomitant decrease of An and MgO in phenocrysts and microlites observed in Trend 1 (Fig. 9f and h) may reflect melt differentiation both in magma chamber (phenocrysts) and during groundmass (microlites) crystallization. The composition of phenocrysts of the BV2958-3 and -4 lavas plot within this trend (Fig. 9).

By contrast, in Trend 2, as the xenocrysts of the dike BV2958-2 illustrate, An and MgO contents in plagioclase phenocrysts are negatively correlated and reach very high ($An_{>70}$, Fig. 9) and low values, respectively. Such a negative An–MgO correlation has already been observed in plagioclases from a MORB cumulate xenolith (EPR 9°50'N: Ridley et al., 2006, Fig. 3). The trend has been reproduced experimentally by considering a diffusion coefficient for MgO that strongly depends on An content (Costa et al., 2003). In this trend, MgO in plagioclase is no longer valuable in estimating MgO in the equilibrium melt. Furthermore, the An-rich plagioclases ($An_{>85}$) are not in equilibrium with any known natural anhydrous basaltic melts (Ridley et al., 2006). Following Panjasawatong et al. (1995), Kohut and Nielsen (2003), and Ridley et al. (2006), such An-rich plagioclase xenocrysts

Fig. 9. An and MgO profiles in plagioclase crystals of the dive BV2958 samples and position of the profile analyses in the An versus MgO diagram. Selected analyses are given in Table 1. Locations of the profiles inside the crystals are shown. Theoretical plagioclase compositions plotted in the An versus MgO diagram are deduced from the host rock analyses, considering the following equilibrium constant of plagioclase-melt exchange reactions for anorthite and albite: $^{Ca-Na}K_D=1.3$ for anhydrous melt (Baker and Eggler, 1987) and $^{Ca-Na}K_D=5.5$ for melt with 2.2 wt.% of H_2O (Sisson and Grove, 1993). MgO content in plagioclase is deduced from the partition coefficient of Mg between plagioclase and melt ($d^{Mg}=0.035$, Ginibre et al., 2002). a–d) Plagioclase xenocrysts of the dyke BV2958-2. To emphasize the large-scale tendencies, a seven-point running average is applied to the MgO data. e and f) Plagioclase phenocrysts of the pillow-lava BV2958-3. g and h) Plagioclase phenocryst of the pillow-lava BV2958-4. R=rim, CM=calcic mantle, Ca-R=calcic rim.

present in anhydrous MORBs would have crystallized in equilibrium with a melt characterized by an unusually high CaO/Na_2O ratio (>8). However, such melts have never been sampled. Since such high An compositions have also been interpreted to be the result of high water contents in the host melt (Hattori and Sato, 1996;



Kuritani, 1998; Ginibre et al., 2002; Landi et al., 2004; Berndt et al., 2005), we prefer to envisage the occurrence of local hydrated areas within a composite magma reservoir beneath the ridge. Such a hypothesis is supported by further petrologic hydration markers found in other samples of the dive BV2958 (clinopyroxene inclusion in plagioclase phenocrysts and fO_2 values in the BV2958-3 and -4 lavas). Consequently, we calculated theoretical compositions of plagioclases crystallizing in equilibrium with BV2958-2, both under anhydrous conditions and with 2.2 wt.% of H_2O in the magma (Fig. 9b and d). Addition of H_2O in the liquid clearly shifts the plagioclase composition toward high An content (from An_{76} to An_{93}, in the studied case) and allows reproducing the An-rich compositions observed in the Trend 2 (up to An_{91}).

6.3. BV2958-2: mushy boundary layer crystallization

The An and MgO profiles are shown in Fig. 9a–d, together with the Ca distribution maps collected in two plagioclases of the BV2958-2 xenolith. MgO contents display short-wavelength fluctuations of variable amplitude. In the core of Xenocryst A, An is quite constant ($An_{77–81}$) but MgO shows great variations (0.17 to 0.27 wt.%, Fig. 9a and b). The core is sharply surrounded by a calcic mantle ($An_{79–86}$) split by large An-poor zones ($An_{74–78}$) where MgO correlates negatively with An. The rims of the crystal have low-An ($An_{50–71}$), low-MgO, and microlite-like compositions. The right side of Xenocryst B includes a small (0.4 mm wide) normally zoned plagioclase crystal (Xenocryst C), composed of an An-rich core ($An_{84–89}$) abruptly cut by less calcic margins ($An_{76–84}$, Fig. 9c). MgO and An in Xenocryst C are negatively correlated as well (Fig. 9c and d). In host Xenocryst B, rims and calcic mantles are still observed, but there the plagioclase core is characterized by a quite calcic ($An_{79–82}$) and MgO-poor inner zone, bounded by An drops. Then, An gradually increases to achieve the calcic mantle composition. Except in the xenocryst rims, An contents of Xenocrysts A, B, and C are higher than for a plagioclase crystallizing from the host melt BV2958-2 under anhydrous conditions (Fig. 9b and d).

Calculation of equilibrium plagioclase compositions suggests that the most An-rich compositions (An_{86} for Xenocryst-A calcic mantles and An_{89} for Xenocryst-C core) can result from the addition of less than 2 wt.% H_2O in the magma. On the other hand, the phenocryst compositions are quite in equilibrium with the host rock, under anhydrous conditions (Fig. 9b and d). H_2O-rich melt compositions may not have prevailed in the whole magma reservoir but may reflect local conditions. The zoning patterns recorded in Xenocrysts A, B, and C could be explained by a mechanical transport through a H_2O gradient. Such a Trend 2-type evolution, extending toward An-rich compositions, has already been observed by Kuritani (1998) in phenocrysts of alkali basalts from the Rishiri stratovolcano. It has been interpreted as resulting from crystallization in a hydrated mushy boundary layer. Beneath spreading ridges, magma chambers are thought to be composite (Sinton and Detrick, 1992). In the thin melt lens, compositions are mostly mafic, as the BV2958-2 bulk rock composition suggests, and quite anhydrous, as usually presumed for MORBs (Michael and Chase, 1987). The melt lens is underlaid by a large mushy crystallization zone, where H_2O-rich compositions can be locally achieved, due to an input of hydrothermal and/or magmatic water expelled from the adjacent rocks. Xenocrysts are thought to have crystallized alternately from these different zones: calcic mantles of Xenocrysts A and B and core of Xenocryst C would have crystallized in the hydrated mushy zone, whereas less calcic compositions would have recorded crystallization in or near the melt lens. The An-poor zones disturbing the calcic mantles might reveal rhythmic crystal motions between both zones. Magma tapping has preferentially sampled the easily removable basaltic liquid from the melt lens, together with a few crystals from locally hydrated areas of the mushy zone. Crystallization after magma eruption has been recorded by the An-poor, microlite-like crystal rims.

6.4. BV2958-3 and BV2958-4: hydration and magma mixing

The plagioclase phenocrysts of the lavas BV2958-3 and -4 present contrasted chemical profiles and distinct An and MgO contents (Trend 1, Fig. 9e–h) with respect to the xenocrysts of the dike BV2958-2 (Trend 2). Thus, they show evidence for different conditions of crystallization. In BV2958-3, Phenocrysts D and E are normally zoned (core with $An_{53–59}$ and rims with $An_{37–50}$) and their Trend 1-type microlite-like compositional variations predominantly reflect post-emplacement crystallization of the host lava. In contrast, Phenocryst F of BV2958-4 exhibits a clear reversal zoning: in the chemical profile made through the bifid termination of the crystal, each branch contains a core ($An_{54–57}$) surrounded by more calcic rims ($An_{57–75}$, Fig. 9g and h).

In the An versus MgO diagram, the profile analyses plot toward lower An than the equilibrium plagioclases crystallizing in anhydrous conditions (Fig. 9f and h). We calculated the mean MgO content and Ca/Na ratio of the

anhydrous melts supposed to be in equilibrium with the cores of Phenocrysts D, E, and F. They are evolved liquids (Ca/Na ~ 0.8 and MgO ~ 3.6 wt.%), with compositions comparable to those of the segregation vesicles or the Cleft dacite. Such calculations, together with the observed inverse zoning, suggest that the core of Phenocryst F would have crystallized in a dacitic magma whereas its calcic rims would equilibrate with a more mafic liquid. This interpretation is consistent with the Ni-rich compositions of the subaphyric and evolved host lavas (BV2958-3 and -4), a feature that we previously interpreted as resulting from a mixing event.

In addition, BV2958-3 and -4 present petrologic evidence for H_2O-influenced crystallization. First, they are some of the few WDB samples in which the augite crystals are systematically included in plagioclase phenocrysts. Such textural relationships are usually indicative of H_2O in magma (Landi et al., 2004). Moreover, fO_2 values, determined from BV2958-3 groundmass Fe–Ti oxides, plot slightly above the FMQ buffer (Fig. 4) and are higher than those of common MORBs (Christie et al., 1986; Bezos and Humler, 2005; Lee et al., 2005). High fO_2 values are the expression of oxidized conditions of crystallization, possibly in connection with relatively high H_2O pressures. Such an interpretation is consistent with the high vesicularity (second boiling) observed in BV2958-3.

The combination of petrologic studies of the dike BV2958-2 (plagioclase xenocrysts) and the overlying pillow-lavas BV2958-3 and -4 (plagioclase phenocrysts, equilibration of Fe–Ti oxide pairs) can be used to track the mechanisms operating in the magma chamber during a limited interval of time. Dacitic residual H_2O-rich melts from the mushy zone, a relic of which is the xenolith observed in BV2958-2, either spread to the whole reservoir or are confined to localized areas. Then, they mix with mafic resident magmas. Such a mixing might explain the Ni-rich intermediate lava compositions (ferrobasalts BV2958-3 and -4) together with the inverse zoning of Phenocryst F. The hydration associated with this mixing event was sufficient to delay plagioclase crystallization and increase fO_2 values but not enough to cause An-rich plagioclase crystallization far away from the mushy zone.

7. An open magma chamber model

The geochemical and petrologic study of the dive BV2958 revealed the occurrence of mixing events in a composite magma reservoir. The chemical characteristics of the samples BV2958-3 and -4 (i.e. Ni-rich compositions), indicative of blending, are shared by other samples from both the Northern Scarp and Parks Plateau, which allows generalizing mixing to all the WBD samples. BV2958-3 and -4 plagioclase compositions have shown that the felsic end-member is probably dacitic. This composition will be represented here by the dacite collected on the Cleft segment (Stakes et al., 2006). The Mg# value of the mafic end-member has to be bracketed between those of (i) the liquid in equilibrium with the analyzed forsteritic olivine Fo_{90} (Mg#=74) and (ii) the intersection of the Ni-Mg# hyperbolic correlation with the line originating from the dacite and bordering downward the Ni-rich compositions (Mg#=66, Fig. 8). Subsequently, linear regressions between Mg# and REE contents (except Sm and Gd, only analyzed in a few samples) have been calculated from 80 fresh, subaphyric, likely cogenetic (variations of La/Nb, Nd/Zr, and La/Yb lesser than 2σ), and Ni-poor lavas from the Northern Scarp. Afterward, these regressions have been used to estimate the REE composition of a mean mafic end-member (Mg#=70). The corresponding calculated pattern shows lower REE concentrations than the Northern Scarp lavas (Fig. 8). The Mg# value of the mafic end-member is close to that of primary MORBs (Kinzler and Grove, 1992; Nielsen et al., 1995), which implies that the corresponding melt has undergone little differentiation subsequently to the replenishment.

Using some Northern Scarp dives through the extrusive unit, further evidence of replenishment is shown by the distribution of Mg# with depth. The interpretation of the Mg# variations with depth might be complicated along the upper part of the scarp. Indeed, the magnetic data (Tivey, 1996) together with the minimal deformation and tilting (Karson et al., 2002) suggest that the uppermost lavas could be emplaced by late flows channeled off-axis. In this case, the contact between the uppermost and underlying lavas represents a time gap (Fig. 10). The closest dives, spaced by less than 3 km, can be considered as sampling equivalent sections of crust as such a distance is in the width range of the axial graben of the Cleft segment (Canales et al., 2005; Stakes et al., 2006). Consequently, these dives will be combined to increase the sampling density and the length of the vertical traverses (Figs. 2 and 10). For each group of selected dives, Mg# is plotted against depth (Fig. 10). The selected dives cover the central part of the Northern Scarp, from 25 to 44.5 km east of the axis. Samples of isotopic group NS2 will not be included in the coming discussion as they are issued from different parental melts.

The Mg# evolution of the previously studied dive BV2958, combined with the dive BN18, is plotted in Fig. 10b. Even if the three other dive groups cross over an oldest crust (Matuyama and Anomaly 2 magnetic

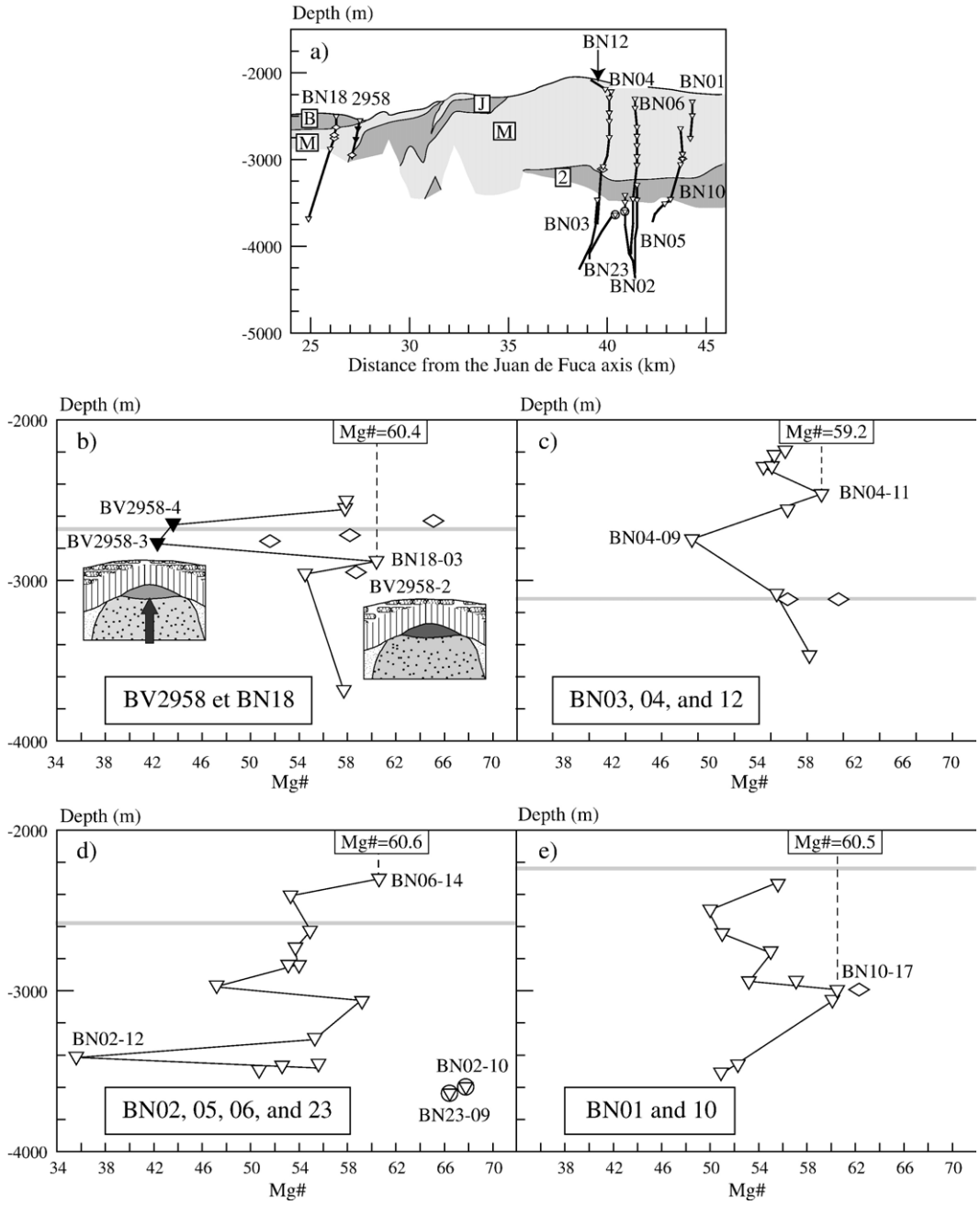


Fig. 10. Evolution of Mg# with depth in extrusive unit for four groups of dives (see text for the selection criteria). a) Position of the selected dives along the Northern Scarp superimposed on the magnetic cross section. b) Dives BV2958 and BN18. Sketches of the proposed model of refilling and mixing are shown (dark gray: mafic magma, light gray: dacitic magma). c) Dives BN03, 04, and 12. d) Dives BN02, 05, 06, and 23. e) Dive BN01 and 10. In each diagram, the unconformity at the base of the uppermost lavas is symbolized by a gray line (Karson et al., 2002) and the name of the key samples and Mg# in the most mafic composition are given. Symbols as in Fig. 5.

periods, Fig. 10a), Mg# varies with depth in a comparable way with, from bottom to top, a change from mafic to intermediate terms followed by a return to mafic compositions. Moreover, the most mafic compositions reached in extrusive samples for each dive are particularly homogeneous ($58.2 \leq Mg\# \leq 60.6$ in 8 samples). The most evolved compositions are either ferrobasalts or evolved basalts with Mg# ranging from 47 to 51 (Fig. 10b–e). These similarities suggest that: (i) replenishment is a widespread event; (ii) this event has

governed the magmatic system over a significant period of time; (iii) the replenishment melt composition remained quite constant.

8. Conclusions

As pointed out by Pollock et al. (2005) using the Blancovin dives, the uppermost lavas that possibly flowed several kilometers away from the axis, tend to be among the most primitive observed along a vertical path. Our data have been used to characterize the time evolution of the geochemistry with more details. We have pointed out that the differentiation degree does not decrease continuously with depth but shows a more complex pattern that can be interpreted as the result of periodic replenishment of the magma reservoir beneath the Cleft axis. In our interpretation, ferrobasalts are produced by a mixing process between dacitic and mafic end-members in such an open and long-lived magma system. The evolved compositions probably result from differentiation in the cooler mushy zones, as Stakes et al. (2006) proposed. Such models cast doubt on the interpretation of Juteau et al. (1995), in which ferrobasalts are viewed as products of closed-system differentiation in short-lived magma reservoirs during the progressive transition from propagation to accretion.

Acknowledgements

Microprobe studies were performed with the help of M. Bohn. Detailed and constructive comments by three anonymous reviewers helped us to improve this manuscript. We also thank Dr. Foley for its editorial assistance. Contribution no. 1035 of the IUEM, European Institute for Marine Studies (Brest, France).

Appendix A. Supplementary data

Supplementary data associated with this article can be found, in the online version, at doi:10.1016/j.lithos.2007.06.009.

References

Andersen, D.J., Lindsley, D.H., 1985. New (and final!) models for the Ti-magnetite/ilmenite geothermometer and oxygen barometer. Abstract AGU 1985 Spring Meeting. Eos Transactions, American Geophysical Union, vol. 66, p. 416.

Baker, D.R., Eggler, D.H., 1987. Compositions of anhydrous and hydrous melts coexisting with plagioclase, augite, and olivine or low-Ca pyroxene from 1 atm to 8 kbar: application to the Aleutian volcanic center of Akta. American Mineralogist 72, 12–28.

Barrat, J.A., Keller, F., Amosse, J., 1996. Determination of rare earth elements in sixteen silicate reference samples by ICP-MS after Tm addition and ion exchange separation. Geostandards Newsletter 20, 133–139.

Berndt, J., Koepke, J., Holtz, F., 2005. An experimental investigation of the influence of water content and oxygen fugacity on differentiation of MORB at 200 MPa. Journal of Petrology 46, 135–167.

Bezos, A., Humler, E., 2005. The $Fe^{3+}/\sum Fe$ ratio of MORB glasses and their implications for mantle melting. Geochimica et Cosmochimica Acta 69, 711–725.

Byerly, G.R., 1980. The nature of differentiation trends in some volcanic rocks from the Galapagos spreading center. Journal of Geophysical Research 85, 3797–3810.

Canales, J.P., Detrick, R.S., Carbotte, S.M., Kent, G.M., Diebold, J.B., Harding, A.J., Babcock, J.M., Nedimovic, M.R., Van Ark, E., 2005. Upper crustal structure and axial topography at intermediate spreading ridges: seismic constraints from the southern Juan de Fuca ridge. Journal of Geophysical Research 110. doi:10.1029/2005JB003630.

Caroff, M., Lagabrielle, Y., Spadea, P., Auzende, J.-M., 1997. Geochemical modeling of nonsteady-state magma chambers: a case study from an ultrafast spreading ridge, East Pacific Rise, 17–19°S. Geochimica et Cosmochimica Acta 61, 4367–4374.

Chadwick, J., Perfit, M.R., Ridley, W.I., Jonasson, I.R., Kamenov, G., Chadwick, W.W.J., Embley, R.W., Le Roux, P., Smith, M.C., 2005. Magmatic effects of the Cobb hot spot on the Juan de Fuca Ridge. Journal of Geophysical Research 110, B03101. doi:10.1029/2003JB002767.

Christie, D.M., Carmichael, I.S.E., Langmuir, C.H., 1986. Oxidation states of mid-ocean ridge basalt glasses. Earth and Planetary Science Letters 79, 397–411.

Cohen, R.S., Evensen, N.M., Hamilton, P.J., O'Nions, R.K., 1980. U–Pb, Sm–Nd and Rb–Sr systematics of Mid-Ocean Ridge Basalt glasses. Nature 283, 149–153.

Costa, F., Chakraborty, S., Dohmen, R., 2003. Diffusion coupling between trace and major elements and a model for calculation of magma residence times using plagioclase. Geochimica et Cosmochimica Acta 67, 2189–2200.

Cotsonika, L.A., Perfit, M.R., Smith, M.C., Kamenov, G.D., Stakes, D.S., Ridley, W.I., Wallace, P., 2005. The occurrence and origin of andesites and dacites from the Southern Juan de Fuca Ridge. Eos, Transactions, American Geophysical Union. Joint Assembly Supplement, vol. 86, pp. 04–V13A.

Cotten, J., Le Dez, A., Bau, M., Maury, R.C., Dulski, P., Fourcade, S., Bohn, M., Brousse, R., 1995. Origin of anomalous rare-earth element and yttrium enrichments in subaerially exposed basalts: evidence from French Polynesia. Chemical Geology 119, 115–138.

Cousens, B.L., Allan, J.F., Leybourne, M.I., Chase, R.L., Van Wagoner, N., 1995. Mixing of magmas from enriched and depleted mantle sources in the northeast Pacific: West Valley segment, Juan de Fuca Ridge. Contributions to Mineralogy and Petrology 120, 337–357.

Dauteuil, O., 1995. Fault pattern form Seabeam processing: the western part of the Blanco Fracture Zone (NE Pacific). Marine Geophysical Researches 17, 17–35.

Davis, A.S., Clague, D.A., 1987. Geochemistry, mineralogy, and petrogenesis of basalts from the Gorda ridge. Journal of Geophysical Research 92, 10476–10483.

Davis, A.S., Clague, D.A., White, W.M., 1998. Geochemistry of basalt from Escabana Trough: evidence for sediment contamination. Journal of Petrology 39, 841–858.

Delaney, J.D.E., Spiess, F.N., Colony, W.E., Karsten, J.L., Kelley, D.S., Nehlig, P., 1987. A complete deep-tow swath map of

south-facing wall of the Blanco Trough, Juan de Fuca region. Eos, Transactions, American Geophysical Union. Fall Meeting Supplement, vol. 68, p. 1509.

Dosso, L., Hanan, B.B., Bougault, H., 1991. Sr–Nd–Pb geochemical morphology between 10°N and 17°N on the Mid-Atlantic Ridge: a new MORB isotope signature. Earth and Planetary Science Letters 106, 29–43.

Dunn, R.A., Toomey, D.R., 2000. Three-dimensional seismic structure and physical properties of the crust and shallow mantle beneath the East Pacific Rise at 9°30'N. Journal of Geophysical Research 105, 23537–23555.

Embley, R.W., Wilson, D.S., 1992. Morphology of the Blanco Transform Fault Zone-NE Pacific: implications for its tectonic evolution. Marine Geophysical Researches 14, 25–45.

Fleutelot, C., 1997. Propagation de segments de dorsales océaniques et modélisation pétro-géochimique de l'évolution des réservoirs magmatiques. Ph.D. dissertation. University of Brest, France.

Gaetani, G.A., DeLong, S.E., Wark, D.A., 1995. Petrogenesis of basalts from the Blanco Trough, northeast Pacific: inferences for off-axis melt generation. Journal of Geophysical Research 100, 4197–4214.

Ginibre, C., Wörner, G., Kronz, A., 2002. Minor- and trace-element zoning in plagioclase: implications for magma chamber processes at Parinacota volcano, northern Chile. Contributions to Mineralogy and Petrology 143, 300–315.

Goldstein, S.J., Murrell, M.T., Janecky, D.R., Delaney, J.R., Clague, D.A., 1991. Geochronology and petrogenesis of MORB from the Juan de Fuca and Gorda ridges by ^{238}U–^{230}Th disequilibrium. Earth and Planetary Science Letters 107, 25–41.

Hart, S.R., Davis, K.E., 1978. Nickel partitioning between olivine and silicate melt. Earth and Planetary Science Letters 40, 203–219.

Hattori, K., Sato, H., 1996. Magma evolution recorded in plagioclase zoning in 1991 Pinatubo eruption products. American Mineralogist 81, 982–994.

Hegner, E., Tatsumoto, M., 1987. Pb, Sr, and Nd isotopes in basalts and sulfides from the Juan de Fuca ridge. Journal of Geophysical Research 92, 11380–11386.

Ito, E., White, W.M., Goepel, C., 1987. The O, Sr–Nd, and Pb isotope geochemistry of Mid-Ocean Ridge Basalts. Chemical Geology 62, 157–176.

Juteau, T., Bideau, D., Dauteuil, O., Manac'h, G., Naidoo, D.D., Nehlig, P., Ondreas, H., Tivey, M.A., Whipple, K.X., Delaney, J.R., 1995. A submersible study in the Western Blanco Fracture Zone, N.E. Pacific: structure and evolution during the last 1.6 Ma. Marine Geophysical Researches 17, 399–430.

Karson, J.A., Maurice, A.T., Delaney, J.R., 2002. Internal structure of uppermost oceanic crust along the Western Blanco Transform Scarp: implications for subaxial accretion and deformation at the Juan de Fuca Ridge. Journal of Geophysical Research 107. doi:10.1029/2000JB000051.

Kinzler, R.J., Grove, T.L., 1992. Primary magmas of Mid-Ocean Ridge Basalts 2. Applications. Journal of Geophysical Research 97, 6907–6926.

Kohut, E.J., Nielsen, R.L., 2003. Low-pressure phase equilibria of anhydrous anorthite-bearing mafic magmas. Geochemistry Geophysics Geosystems 4, 1057. doi:10.1029/2002GC000451.

Kuritani, T., 1998. Boundary layer crystallization in a basaltic magma chamber: evidence from Rishiri volcano, northern Japan. Journal of Petrology 39, 1619–1640.

Lagabrielle, Y., Cormier, M.-H., 1999. Formation of large summit troughs along the East Pacific Rise as collapse calderas: an evolutionary model. Journal of Geophysical Research 104, 12971–12988.

Landi, P., Métrich, N., Bertagnini, A., Rosi, M., 2004. Dynamics of magma mixing and degassing recorded in plagioclase at Stromboli (Aeolian Archipelago, Italy). Contributions to Mineralogy and Petrology 147, 213–227.

Le Bas, M.J., Le Maitre, R.W., Streckeisen, A., Zanettin, B., 1986. A chemical classification of volcanics rocks based on the total alkali-silica diagram. Journal of Petrology 27, 745–750.

Lee, C.T.A., Leeman, W.P., Canil, D., Li, Z.-X.A., 2005. Similar V/Sc systematics in MORB and arc basalts: implications for the oxygen fugacities of their mantle source region. Journal of Petrology 46, 2313–2336.

Lepage, L.D., 2003. ILMAT: an Excel worksheet for ilmenite-magnetite geothermometry and geobarometry. Computers & Geosciences 29, 673–678.

Manac'h, G., Lécuyer, C., Juteau, T., 1999. A fluid inclusion and stable isotope study of hydrothermal circulation in a transform zone: Western Blanco Depression, northeast Pacific. Journal of Geophysical Research 104. doi:10.1029/1998JB900069.

Michael, P.J., Chase, R.L., 1987. The influence of primary magma composition, H_2O and pressure on Mid-Ocean Ridge Basalt differentiation. Contributions to Mineralogy and Petrology 96, 245–263.

Middlemost, E.A.K., 1989. Iron oxydation ratios, norms and the classification of volcanic rocks. Chemical Geology 77, 19–26.

Naidoo, D.D., 1998. Accretion of the upper oceanic crust. Ph.D. dissertation. University of Washington, Seattle.

Nielsen, R.L., Crum, J., Bourgeois, R., Hascall, K., Forsythe, L.M., Fisk, M.R., Christie, D.M., 1995. Melt inclusions in high-An plagioclase from the Gorda Ridge: an example of the local diversity of MORB parent magmas. Contributions to Mineralogy and Petrology 122, 34–50.

Niu, Y., Bideau, D., Hekinian, R., Batiza, R., 2001. Mantle compositional control on the extent of mantle melting, crust production, gravity anomaly, ridge morphology, and ridge segmentation: a case study at the Mid-Atlantic Ridge 33-35°N. Earth and Planetary Science Letters 186, 383–399.

Panjasawatong, Y., Danyushevsky, L.V., Crawford, A.J., Harris, K.L., 1995. An experimental study of the effects of melt composition on plagioclase-melt equilibria at 5 and 10 kbar: implications for the origin of high An plagioclase in arc and MORB magmas. Contributions to Mineralogy and Petrology 118, 420–435.

Pollock, M.A., Klein, E.M., Karson, J.A., Tivey, M.A., 2005. Temporal and spacial variability in the composition of lavas exposed along the Western Blanco Transform Fault. Geochemistry Geophysics Geosystems 6. doi:10.1029/2005GC001026.

Rhodes, J.M., Morgan, C., Liias, R.A., 1990. Geochemistry of Axial Seamount lavas: magmatic relationship between the Cobb hotspot and the Juan de Fuca ridge. Journal of Geophysical Research 95, 12713–12733.

Ridley, W.I., Perfit, M.R., Smith, M.C., Fornari, D.J., 2006. Magmatic processes in developing oceanic crust revealed in a cumulate xenolith collected at the East Pacific Rise, 9°50'N. Geochemistry Geophysics Geosystems 7, Q12O04. doi:10.1029/2006GC001316.

Roeder, P.L., Emslie, R.F., 1970. Olivine-liquid equilibria. Contributions to Mineralogy and Petrology 29, 275–289.

Singh, S.C., Kent, G.M., Collier, J.S., Harding, A.J., Orcutt, J.A., 1998. Melt to mush variations in crustal magma properties along the ridge crest at the southern East Pacific Rise. Nature 394, 874–878.

Sinton, J.M., Detrick, R.S., 1992. Mid-ocean ridge magma chambers. Journal of Geophysical Research 97, 197–216.

Sinton, J.M., Wilson, D.S., Christie, D.M., Hey, R.N., Delaney, J.R., 1983. Petrologic consequences of ridge propagation on oceanic

spreading ridges. Earth and Planetary Science Letters 62, 193–207.

Sinton, J.M., Smaglik, S.M., Mahoney, J.J., Macdonald, K.C., 1991. Magmatic processes at superfast spreading mid-ocean ridges: glass compositional variations along the East Pacific Rise 13°–23°S. Journal of Geophysical Research 96, 6133–6155.

Sisson, T.W., Grove, T.L., 1993. Experimental investigations of the role of H_2O in calc-alkaline differentiation and subduction zone magmatism. Contributions to Mineralogy and Petrology 113, 143–166.

Smith, J.V., Brown, W.L., 1988. Feldspar minerals. 1. Crystal structures, physical, chemical, and microtextural properties. Springer Verlag, Berlin. 828p.

Smith, M.C., Perfit, M.R., Jonasson, I.R., 1994. Petrology and geochemistry of basalts from the southern Juan de Fuca ridge: controls on the spatial and temporal evolution of mid-ocean ridge basalts. Journal of Geophysical Research 99, 4787–4812.

Smith, S.E., Casey, J.F., Bryan, W.B., Dmitriev, L., Silantyev, S., Magakyan, R., 1998. Geochemistry of basalts from the Hayes Transform region of the Mid-Atlantic ridge. Journal of Geophysical Research 103, 5305–5329.

Stakes, D.S., Perfit, M.R., Tivey, M.A., Caress, D.W., Ramirez, T.M., Maher, N., 2006. The Cleft revealed: geologic, magnetic, and morphologic evidence for construction of upper oceanic crust along the southern Juan de Fuca Ridge. Geochemistry Geophysics Geosystems 7. doi:10.1029/2005GC001038.

Sun, S.S., McDonough, W.F., 1989. Chemical and isotopic systematics of oceanic basalts: implication for mantle composition and processes. In: Saunders, A.D., Norry, M.J. (Eds.), Magmatism in the Ocean Basins. Geological Society Special Publication, London, pp. 313–345.

Tivey, M.A., 1994. Fine-scale magnetic anomaly field over the southern Juan de Fuca ridge: axial magnetization low and implications for crustal structure. Journal of Geophysical Research 99, 4833–4855.

Tivey, M.A., 1996. Vertical magnetic structure of ocean crust determined from near-bottom magnetic field measurements. Journal of Geophysical Research 101, 20275–20296.

Tivey, M.A., Johnson, H.P., Fleutelot, C., Hussenoeder, S.A., Lawrence, R., Waters, C., Wooding, B., 1998. Direct measurement of magnetic reversal polarity boundaries in a cross-section of oceanic crust. Geophysical Research Letters 25, 3631–3634.

Volpe, A.M., Goldstein, S.J., 1993. ^{226}Ra–^{230}Th disequilibrium in axial and off-axis mid-ocean ridge basalts. Geochimica and Cosmochimica Acta 57, 1233–1241.

Wendt, J.I., Regelous, M., Niu, Y., Hékinian, R., Collerson, K.D., 1999. Geochemistry of lavas from the Garrett Transform Fault: insights into mantle heterogeneity beneath the eastern Pacific. Earth and Planetary Science Letters 173, 271–284.

White, W.M., Hofmann, A.W., Puchelt, H., 1987. Isotope geochemistry of Pacific Mid-Ocean Ridge Basalts. Journal of Geophysical Research 92, 4881–4893.

Wilson, D.S., 1992. Focused mantle upwelling beneath mid-ocean ridges: evidence from seamount formation and isostatic compensation of topography. Earth and Planetary Science Letters 113, 41–55.

Wilson, D.S., Hey, R.N., Nishimura, C., 1984. Propagation as a mechanism of reorientation of Juan de Fuca Ridge. Journal of Geophysical Research 89, 9215–9225.